Review

Xingliang Li, Qiaojing Xu, Lingling Yan, Chengchao Ren, Biao Shi, Pengyang Wang, Sayantan Mazumdar, Guofu Hou*, Ying Zhao* and Xiaodan Zhang*

Silicon heterojunction-based tandem solar cells: past, status, and future prospects

https://doi.org/10.1515/nanoph-2021-0034
Received January 28, 2021; accepted April 20, 2021;
published online May 18, 2021

Abstract: Due to stable and high power conversion efficiency (PCE), it is expected that silicon heterojunction (SHJ) solar cells will dominate the photovoltaic market. So far, the highest PCE of the SHJ-interdigitated back contact (IBC) solar cells has reached 26.7%, approximately approaching the theoretical Shockley–Queisser (SQ) limitation of 29.4%. To break through this limit, multijunction devices consisting of two or three stacked subcells have been developed, which can fully utilize the sunlight by absorbing different parts of the solar spectrum. This article provides a comprehensive overview of current research on SHJ-based tandem solar cells (SHJ-TSCs), including perovskite/SHJ TSCs and III–V/SHJ TSCs. Firstly, we give a brief introduction to the structures of SHJ-TSCs, followed by a discussion of fabrication processes. Afterwards, we focus on various materials and processes that have been explored to optimize the electrical and optical performance. Finally, we highlight the opportunities and challenges of SHJ-TSCs, as well as personal perspectives on the future development directions in this field.

Keywords: III–V/SHJ tandem solar cell; electrical and optical performance; perovskite/SHJ tandem solar cell; SHJ solar cell.

1 Introduction

Crystalline silicon solar cells have dominated the photovoltaic market for decades. System components including installation, cabling, and inverters account for the main cost of photovoltaics, because these costs are area-dependent. Improving the power conversion efficiency (PCE) is the most powerful means to reduce the levelized cost of electricity. Silicon heterojunction (SHJ) solar cells include c-Si/a-Si [1–7], c-Si/poly-Si [8–11], c-Si/SiO_x [12–17], and c-Si/MoO_x [18, 19] heterojunctions solar cells. SHJ solar cells represent the new research direction due to their high performance. So far, the world record of 26.7% cell efficiency was set by Kaneka in 2017 [5]. It uses an SHJ structure combined with an interdigitated back-contact (IBC). However, this efficiency is only 2.7% lower than the theoretical efficiency limit of 29.4% for silicon single-junction solar cells [20]. This means it is really close to its performance limit. There is an urgent need of novel methods to be adopted.

A well-known strategy to overcome the Shockley–Queisser (SQ) theoretical efficiency limit is to employ multijunction architecture. In these devices, a wide band gap top cell absorbs high-energy photons, and a narrow band gap bottom cell absorbs low-energy photons. This structure can minimize the thermalization losses and improve the utilization of the solar spectrum. According to simulation results, the maximum limiting PCE of dual-junction silicon based tandem solar cells (TSCs) is 45%, and that of triple-junction silicon based TSCs is 50% [21, 22]. For silicon based TSCs, various top cell materials

***Corresponding authors: Guofu Hou, Ying Zhao and Xiaodan Zhang,** Institute of Photoelectronic Thin Film Devices and Technology, Renewable Energy Conversion and Storage Center, Solar Energy Conversion Center, Nankai University, Tianjin 300350, P. R. China; Key Laboratory of Photoelectronic Thin Film Devices and Technology of Tianjin, Tianjin 300350, P. R. China; Engineering Research Center of Thin Film Photoelectronic Technology of Ministry of Education, Tianjin 300350, P. R. China; and Collaborative Innovation Center of Chemical Science and Engineering (Tianjin), Tianjin 300072, P. R. China, E-mail: xdzhang@nankai.edu.cn (X. Zhang), gfhou@nankai.edu.cn (G. Hou), zhaoygds@nankai.edu.cn (Y. Zhao). https://orcid.org/0000-0002-0522-5052 (X. Zhang)
Xingliang Li, Qiaojing Xu, Lingling Yan, Chengchao Ren, Biao Shi, Pengyang Wang and Sayantan Mazumdar, Institute of Photoelectronic Thin Film Devices and Technology, Renewable Energy Conversion and Storage Center, Solar Energy Conversion Center, Nankai University, Tianjin 300350, P. R. China; Key Laboratory of Photoelectronic Thin Film Devices and Technology of Tianjin, Tianjin 300350, P. R. China; Engineering Research Center of Thin Film Photoelectronic Technology of Ministry of Education, Tianjin 300350, P. R. China; and Collaborative Innovation Center of Chemical Science and Engineering (Tianjin), Tianjin 300072, P. R. China. https://orcid.org/0000-0003-3463-9198 (S. Mazumdar)

Open Access. © 2021 Xingliang Li et al., published by De Gruyter. This work is licensed under the Creative Commons Attribution 4.0 International License.

have been endeavored, but current research focuses on III–V and perovskite semiconductors. III–V solar cells have been known for their high efficiency and excellent reliability, which reduces the invest risk and improves the stability of tandem modules. A PCE of 35.9% was reported for a mechanically stacked four terminal GaInP/GaAs/Si tandem device [23]. This is the highest PCE of silicon based TSCs. Meanwhile, perovskite solar cell is another ideal candidate for SHJ-based tandem solar cells (SHG-TSCs) due to its tunable bandgap, easy fabrication, and high PCE of 25.5% [24]. Using a low temperature solution method, perovskite solar cells can be well compatible with c-Si/a-Si SHJ solar cell. Record one-sun PCE of 29.5% has been achieved for two terminal perovskite/SHJ TSC by Oxford PV [25]. However, the lager V_{oc} loss of nonradiative recombination and the high sensitivity of perovskite to low levels of humidity, remain as significant challenges that require further research and development.

This article reviews current research activities that center on perovskite/SHJ TSCs and III–V/SHJ TSCs. The text of this article is divided into six parts: Section 2 discusses several structures related to the SHJ-TSCs, as well as fabrication strategies that have been developed for achieving ideal SHJ-TSCs. The following three sections thoroughly illustrate these strategies with specific examples. The final section concludes with personal comments on the directions of future research on such new solar cells.

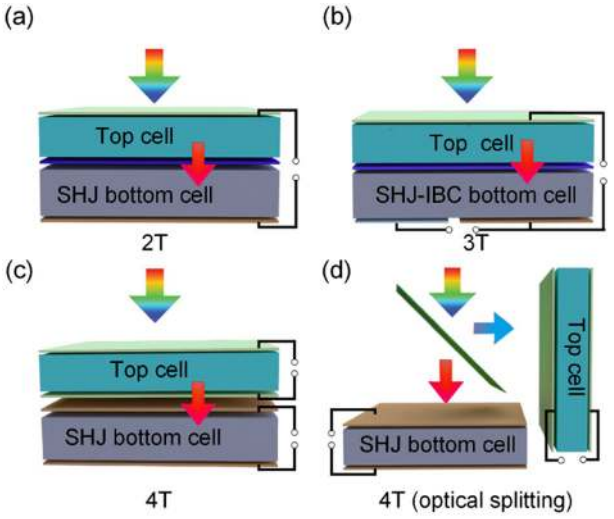

Figure 1: Structural sketches of four kinds of tandem solar cells (TSCs).
(a) Two-terminal tandem device with tunnel junction (TJ), (b) Three-terminal tandem device, (c) Four-terminal tandem device, and (d) Four-terminal optical splitting tandem device.

2 Design consideration for TSCs

2.1 The structure of TSCs

SHJ-TSCs mitigate carrier thermalization losses by using several subcells with different bandgaps. Figure 1 illustrates four different SHJ-TSCs structures. As shown in Figure 1(a), two terminal (2T) devices use a tunnel junction or transparent conductive adhesive to connect the two sub cells. 2T devices have advantages in module integration. This is because 2T devices can be connected in standard series or parallel with little space between the cells [26]. In addition, 2T devices cut down the parasitic absorption by removing the intermediate electrode. So far, all industrially scaled multi-junction solar cells use 2T structure. The fabrication of 2T devices faces three major challenges: current matching, high performance recombination junction and performance losses under varying spectra [27]. Among these factors, tunnel junction plays a key role in obtaining high efficiency by providing a low electrical resistance and high optical transmittance interlayer between the subcells. It is expected that 2T devices will be favorable for future applications with the solution of these problems.

In 3T configurations, the two subcells can be connected by a tunnel junction or recombination layer or wiring [28–31]. The third electrode can be formed at the interface of the top cell and bottom cell, and the third electrode can extract additional generated power by the variation in solar radiance. In addition, when the IBC bottom cell is used, the third electrode can also be formed at the rear side of the bottom cell (Figure 1(b)). Theoretically, 3T devices enable the same performance as 4T devices. For example, Schnabel et al. used IBC bottom cell and GaInP top cell, yielding a PCE of 27.3% for 3T TSC [32].

For 4T configurations, there are two typical structures: mechanically stacked (Figure 1(c)) and optical splitting 4T tandem devices (Figure 1(d)). 4T configuration eliminates the need for recombination junction and requires neither current matching nor processing compatibility between subcells, hence it offers a more flexible option. The two subcells are subjected to optical coupling but they are electrically independent. Each sub cell can be fabricated independently, regardless of fabrication methods and processes. Therefore, the efficiency of each sub cell can be maximized. However, due to the parasitic absorption and resistance from intermediate electrode, significant optical and electrical losses are inevitable. Meanwhile, the complexity of fabricating these devices and implementing them into modules impede their application. Therefore, 4T devices have not been found any practical applications, until now.

2.2 Band gap matching and optoelectronic performance optimization

The theoretical SQ efficiency limit for single junction solar cells with a bandgap of 1.34 eV is 33.7% [33]. So far, the maximum reported efficiency of GaAs with a bandgap of 1.42 eV is 29.1% (Figure 2(a)). As shown in Figure 2(b), the highest V_{oc} of perovskite solar cell with a bandgap of 1.75 eV is 1.24 V [37]. Because of band gap energy and nonradiative voltage loss, the V_{oc} deficits of perovkite solar cell are much higher than GaInP and GaAs solar cell. The champion cell based on wide band gap *n*–*i*–*p* perovskite solar cell now has a PCE of 21.6% [38], a significant gap from the SQ efficiency limit. To break this efficiency limitation, one must rely on the optimized multijunction architecture.

The bandgap combination is an essential requisite for the successful fabrication of SHJ-TSCs. As shown in Figure 2(c), the PCEs of four types of SHJ-TSCs are advancing significantly in past six years. So far, the record PCEs of mechanical stacking GaInP/SHJ and GaAs/SHJ are 32.5 and 32.8%, respectively. By detailed balance model with precise ab initio calculations, the optimal top cell bandgaps of 2T and 4T SHJ-TSCs are 1.73 and 1.81 eV (Figure 2(d)–(e)), respectively [21]. And the PCE of 2T and 4T SHJ-TSCs can exceed 45%, which is close to theoretical maximum of 46%. As shown in Figure 2(f), the PCE increase with the number of *pn* junctions. However, once the number of subcells exceeds three, the gain of PCE for additional sub-cell will become smaller. For triple-junction (3J) tandem devices with SHJ bottom cell, the optimal bandgap combination of top and middle cell is 2.01 and 1.5 eV, respectively. Theoretically, the PCE of triple-junction (3J) Si based TSCs can exceed 50% [36]. However, high quality materials with bandgaps of 2.01 and 1.5 eV are difficult to fabricate, and $Ga_{0.51}In_{0.49}P$(1.91 eV)/$Al_{0.06}Ga_{0.94}As$ (1.51 eV) is a good alternative to be the top and middle cell on SHJ. According to the theoretical simulation, a maximum PCE of GaInP/GaAs/Si is close to 44%. The world-record PCE of GaInP/GaAs/Si was lower

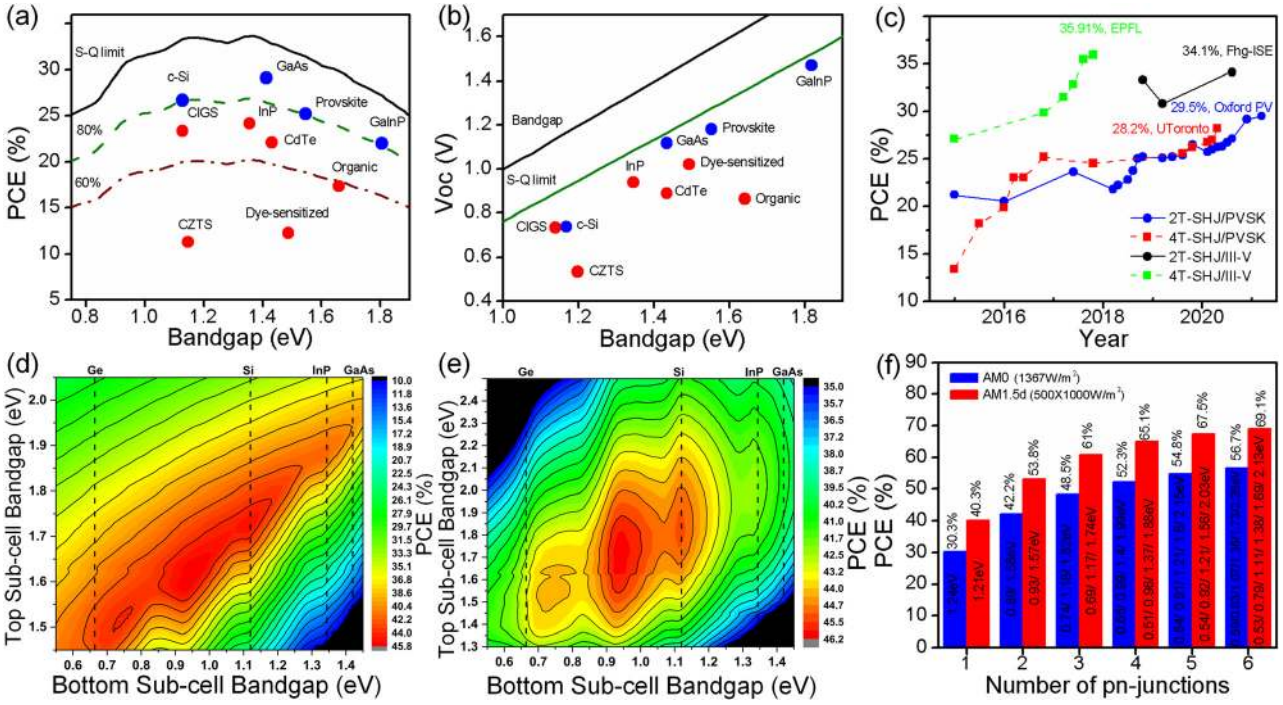

Figure 2: (a) Theoretical Shockley–Queisser (SQ) detailed-balance efficiency limit for single junction solar cell as a function of band gap (solid line). The green and red dashed lines represent 80 and 60% SQ efficiency limit, respectively [34]. The red and blue spheres show the record efficiency of different materials [24]. All data are for standard AM1.5 illumination at 1000 W/m^2. (b) Open-circuit voltage V_{oc} as a function of band gap is shown for reference. The area indicated by the two-way arrow is the voltage gap $V_g - V_{SQ}$ [35]. Copyright 2019, Springer Nature. The red and blue spheres represent the record V_{oc} of different materials [24]. (c) Efficiency evolution of silicon heterojunction (SHJ)-based TSCs: 2T perovskite/SHJ, 2T III–V/SHJ, 4T perovskite/SHJ, 4T III–V/SHJ. (see Tables 1–3 for references). (d) Maximum efficiency contours for dual junction 4T tandems sunder 1 sun AM1.5G [21]. Copyright 2015, IEEE. (e) Maximum efficiency contours for dual junction 2T tandems sunder 1 sun AM1.5G [21]. Copyright 2015, IEEE. (f) Theoretical efficiency limit for multijunction solar cells corresponding to the number of pn-junctions. The blue and red bars represent the solar spectrum of AM0 (1367 W/m^2) and AM1.5d (500 × 1000 W/m^2) [36]. Copyright 2018, Elsevier.

than 36%, far from reaching the theoretical limit [23]. Further improvements in the future are crucial.

3 SHJ bottom cells

As shown in Figure 3(a), typical SHJ solar cell is c-Si/a-Si heterojunction solar cell, also named heterojunction with intrinsic thin-layer cell (HIT) [1–6]. HIT solar cell is commonly used bottom cells in perovskite/Si TSCs. This selection can be attributed to a number of scenarios that may include: (1) An ultrathin hydrogenated amorphous silicon layer is used in HIT to realize excellent surface passivation (Figure 3(b)) [41]. The open-circuit voltage of HIT is as high as 750 mV [3], which is very close to Auger-limited 761 mV with the similar thickness. (2) The transparent electrode of HIT is usually tin-doped indium oxide (ITO), which is a good substrate and recombination layer for perovskite top cell [42]. (3) The HIT cell has good near infrared (NIR) response, which can reduce the optical loss of TSCs. However, HIT cell has temperature limits [41]. A HIT solar cell is not suitable for 2T III–V/Si TSCs because the GaAs substrate is chemically etched. When encountering sulfuric acid, hydrochloric acid and ammonia solution etching, HIT solar cell will degrade. Therefore, other heterojunction structures that replace the c-Si/a-Si heterojunction have attracted the interest of researchers.

New efficient SHJ solar cells may include double side tunnel oxide passivating contacts(TOPCon) solar cell [8, 9], polycrystalline silicon on oxide (POLO) passivating contacts solar cell [10, 11], Silevo Triex solar cell [7], and dopant-free asymmetric heterocontacts (DASH) solar cells [43, 44]. Among this, TOPCon may replace HIT with its high efficiency and temperature stability. So far, most high efficiency 2T III–V/Si TSCs use TOPCon as bottom cell [45–47]. For instance, a record PCE of 34.1% has been achieved for a wafer bonding GaInP/GaAs/Si TSC with a TOPCon bottom cell [47]. Polysilicon/SiO_x passivating contacts provide an ideal design to obtain full-area carrier-collecting junctions [48]. This full-area contact avoids the lateral transport of charge carrier, enables the use of higher resistivity wafers (Figure 3(b)). TOPCon is resistant to light-activated degradation. The annealing temperature above 800 °C form polysilicon contacts make it compatible with the high temperature process of III–V or perovskite top cells. However, the p^+ polysilicon contacts of TOPCon are

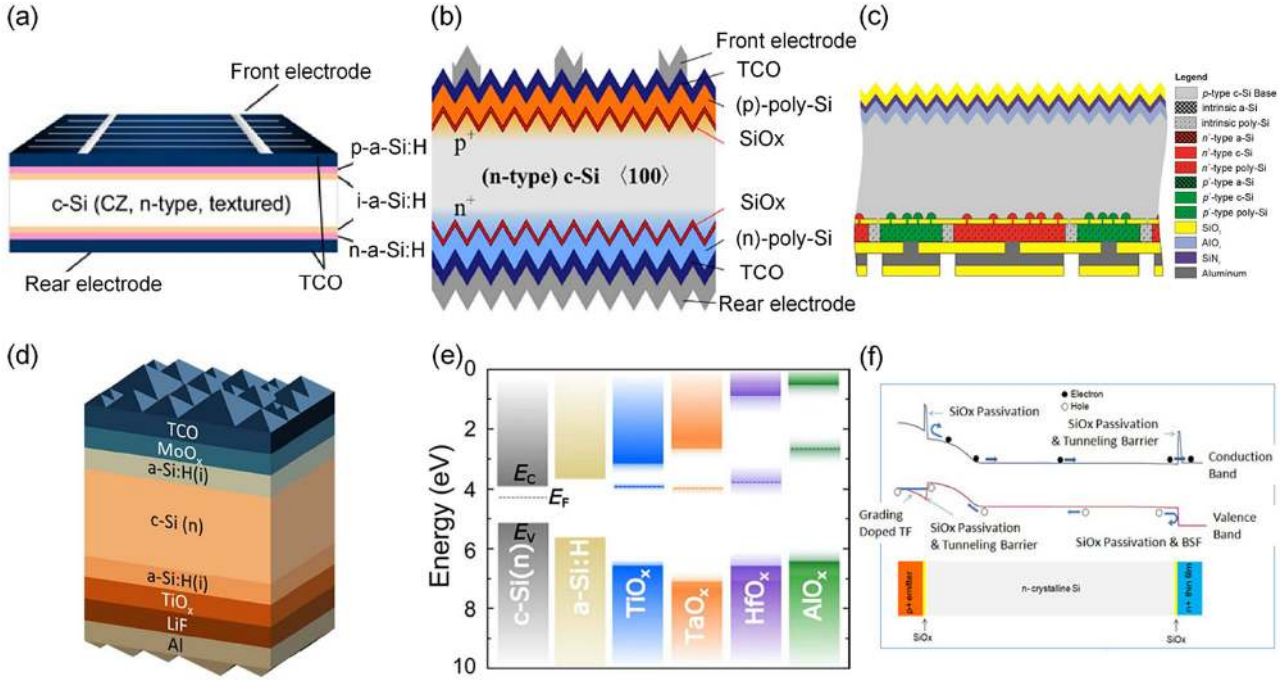

Figure 3: (a) c-Si/a-Si heterojunction solar cell (HIT) with an efficiency of 24.7% [3]. Copyright 2014, IEEE. (b) Schematic cross sections of c-Si/poly-Si heterojunction solar cell (Topcon) [39]. Copyright 2018, Elsevier. (c) Schematic cross-section of the c-Si/poly-Si heterojunction solar cell with interdigitated back contact structure (POLO-IBC) [10]. Copyright 2018, Elsevier. (d) Cross-sectional schematic drawing of dopant-free asymmetric heterocontacts solar cells (DASH) [40]. Copyright 2018, Elsevier. (e) Potential band position of the electron heterocontact materials for DASH solar cell [40]. Copyright 2018, Elsevier. (f) Band diagram of a Silevo Triex solar cell [7]. Copyright 2018, American Chemical Society.

difficult to optimize. This may be due to excessively large valence band offsets between p^+ polysilicon and the silicon wafer [41].

4T SHJ-TSCs usually use polycrystalline silicon on oxide-interdigitated back contact (POLO-IBC) cell as bottom cell. Carrier selective junctions are formed by creating polycrystalline silicon-rich layers on ultrathin silicon oxide films [10, 11]. The pinhole density in interfacial oxide films of POLO junction plays a key role in determining the electrical properties [10, 11]. As shown in Figure 3(c), Haase et al. [10] optimized the layer-selective laser ablation process of SiO_2 and obtained a saturation current density of 2 $fA \cdot cm^{-2}$ on *n*-type POLO. In this approach, the device exhibited a PCE of 26.1% with a V_{oc} of 733 mV. Rienacker et al. prepared GaInP/GaAs//Si triple-junction cell with POLO-IBC bottom cell and achieved a certified PCE of 35.4% [49].

Compared to HIT concept, which suffers parasitic absorption in the window layer, the DASH cells, featuring wide band gap carrier-selective materials on opposite sides, delivers lower current losses in the blue spectrum (Figure 3(e)). Besides, DASH removes the limitations of doped amorphous silicon layers and reduces the recombination-active defects caused by excessive dopant. Therefore, DASH opens a wider optical and electrical parameter space to optimize different solar cell components. Using MoO_x and LiF_x based heterocontacts with a-Si:H passivation layers, Bullock et al. obtained a PCE of 20.7% efficient DASH solar cell (Figure 3(d)) [40]. Based on the concept of metal–insulator–semiconductor, Silevo Triex cell is a proprietary configuration that combines a tunnel oxide junction with doped a-Si:H film emitter layers on silicon wafers. With high quality passivation of ultrathin SiO_x layers, excess carriers can be collected at the emitter by quantum tunneling (Figure 3(f)). By optimizing key processes to improve passivation, junction quality, and shading effects, Heng et al. achieved a PCE of 23.1% [7]. Compared with HIT bottom cell, Silevo Triex cell has higher FF and J_{sc}. Because of less parasitic absorption and carrier recombination, Silevo Triex can be used as bottom cell for TSCs. However, the PCE of Silevo Triex cell is still lower than that of HIT, which limits the application in TSCs.

4 Perovskite/SHJ TSCs

Perovskite/SHJ TSCs have shown PCEs soaring from 13.7% to over 29.5% within merely six years' research and development. Tables 1 and 2 show the evolution of the 2T and 4T perovskite/SHJ TSCs, respectively. Perovskite is typically originated from a 3D crystal structure consisting of three primary ions with a stoichiometry of ABX_3, where A = methylammonium (MA), formamidinium (FA), cesium (Cs), or rubidium (Rb); B = lead (Pb) or tin (Sn); X = iodine (I), bromine (Br), or chlorine (Cl). The crystalline ABX_3 structure can be described as a specifical 3D sublattice in which A^+ is surrounded by BX_6 octahedra. So far, the hybrid perovskite compounds are prepared with either MA or FA as the A cation. By interchanging the above cations [77–86], metals [87], and halides [88, 89], the band gap of perovskite can be adjusted in the range of 1.15–3.06 eV. Organic–inorganic lead halide perovskite solar cells exhibit many advantages that make them attractive for using as top cells in SHJ-TSCs [42, 51–67, 86–89].

4.1 History

As shown in Figure 4(a), early designs for 2T perovskite/SHJ TSCs relied on double side planar SHJ bottom cell, which resulted in significant optical losses. Werner et al. employed double side planar SHJ as bottom cell, yielding a PCE of 19.2% for 2T TSC (Figure 4(b)). Because the reflectance and parasitic absorption losses, the external quantum efficiency (EQE) current density of bottom cell was only 15.6 $mA \cdot cm^{-2}$. An improved structure based on rear side textured SHJ bottom cell can mitigate these losses. SHJ bottom cell with front side planar is compatible with existing solution-based spin-coating perovskite fabrication processes. However, this configuration leads to strong front surface reflection losses and poor light trapping, especially in the NIR area where SHJ bottom cell absorbs weakly [60]. Currently, the best device with rear side textured SHJ exhibits a total cumulative current of 39.6 $mA \cdot cm^{-2}$ [50] (Figure 4(c)), a value that is lower than that of double side textured SHJ-TSCs (40.4 $mA \cdot cm^{-2}$).

Various textured light management structures on the front side have been employed to fully harvest the high photocurrent. For example, McGehee et al. [61] used pyramidal textured polydimethylsiloxane (PDMS) to reduce reflection loss. The EQE current density of perovskite top cell increased by 1 $mA \cdot cm^{-2}$. But the EQE current density of SHJ bottom cell decreased due to PDMS layer was incapable in reducing reflection at longer wavelengths. Textured antireflection foil is another effective way to increase the photocurrent of tandem devices. With antireflection foils, the EQE current density gain of perovskite top cell exceeds 2 $mA \cdot cm^{-2}$ [57]. The reflection loss is reduced to 2.5 $mA \cdot cm^{-2}$. However, the effectiveness of antireflection foils will be impaired during encapsulation [56]. The high processing costs of atomically smooth surfaces makes it difficult as candidate for practical application in SHJ-TSCs.

Table 1: Summary of the optoelectronic parameters of the 2T perovskite/SHJ TSCs.

Si bottom cell	Perovskite top cell	*Eg* (eV)	Recombination layer	Area (cm^2)	V_{OC} (V)	J_{SC} (mA/cm^2)	FF (%)	Eff. (%)	Research institution	Year
Front planar SHJ	$Cs_{0.05}(FA_{0.77}MA_{0.23})_{0.95}Pb(I_{0.77}Br_{0.23})_3$	1.68	ITO	1.0599	1.9	19.26	79.52	29.15	HZB/KTU [50]	2020
Textured SHJ	$(Cs_{0.06}FA_{0.78}MA_{0.16})$ Pb $(Br_{0.17}I_{0.83})_3$	1.64	ITO	1.43	1.8	18.81	77.5	26.3	Tor Vergata- [51]	2020
Front planar SHJ	$Cs_{0.75}MA_{0.22}Pb(I_{0.82}Br_{0.15}Cl_{0.03})_3$	1.67	ITO	1	1.876	18.55	74.85	26.05	CUB/NREL/USTC/SU/ASU [52]	2020
Textured SHJ	$Cs_{0.1}MA_{0.9}Pb(I_{0.9}Br_{0.1})_3$	–	ITO	0.49	1.82	19.2	75.3	26.2	UNC/ASU- [53]	2020
Front planar SHJ	$FA_{0.65}MA_{0.2}Cs_{0.15})$ $Pb(I_{0.8}Br_{0.2})_3$	1.68	ITO	0.188	1.756	19.1	79.2	26.7	KAIST/NU/SNU/NREL- [54]	2020
Front planar SHJ	$Cs_{0.05}(MA_{0.83}FA_{0.17})$ $Pb(I_{0.83}Br_{0.17})_3$	–	ITO	0.7709	1.77	19.22	76.6	26	HZB/TU/e/TUB- [55]	2020
Textured SHJ	$Cs_{0.05}MA_{0.15}FA_{0.8}PbI_{2.25}Br_{0.75})$	1.68	ITO	0.832	1.7932	19.08	75.1	25.7	UToronto/KAUST/NREL/USD [56]	2020
Front planar SHJ	$Cs_{0.05}(MA_{0.17}FA_{0.83})$ $Pb_{1.1}(I_{0.83}Br_{0.17})_3$	1.66	ITO	0.81	1.76	19.4	77	26.5	HZB/ULJ [57]	2019
Front planar SHJ	$Cs_{0.05}(FA_{0.83}MA_{0.17})_{0.95}Pb(I_{1-}xBr_x)_3$	1.63	ITO	0.092	1.79	19.04	74.6	25.43	HZB [42]	2019
Front planar SHJ	$Cs_{0.15}(FA_{0.83}MA_{0.17})_{0.85}Pb(I_{0.8}Br_{0.2})_3$	1.64	ITO	0.49	1.8	17.8	79.4	25.4	UNL/UNC/ASU/CAS [58]	2019
Front Planar SHJ	$Cs_{0.17}FA_{0.83}PbI_{0.83}Br_{0.17}$	1.63	ITO	57.4	1.723	17.48	75	22.6	CSEM/EPFL- [59]	2019
Textured SHJ	$FA_{0.9}Cs_{0.1}PbBr_{0.325}I_{2.675}$	1.6	nc-Si	1.42	1.788	19.5	73.1	25.2	EPFL/CSEM [60]	2018
Front planar SHJ	$FA_{0.75}Cs_{0.25}Pb(I_{0.8}Br_{0.2})_3$	1.68	ITO	1	1.77	18.4	77	25	SU/ASU/TCD- [61]	2018
Planar SHJ	$Cs_{0.08}FA_{0.74}MA_{0.18}Pb(I_{0.88}Br_{0.12})_3$	1.65	ITO	0.13	1.78	17.82	75	23.73	NKU [62]	2018
Front Planar SHJ	$Cs_{0.19}MA_{0.81}PbI_3$	1.58	nc-Si	0.25	1.75	16.8	77.5	22.8	EPFL/CSEM [63]	2018
Front planar SHJ	$Cs_{0.19}MA_{0.81}PbI_3$	1.58	nc-Si	0.25	1.751	16.8	77.5	22	EPFL/CSEM[63]	2018
Front planar SHJ	$CsFAPbI_{3-x}Br_x$	1.63	nc-Si	12.96	1.769	16.5	65.4	19.1	EPFL/CSEM [63]	2018
Front planar SHJ	$FA_{0.83}Cs_{0.17}Pb(I_{0.83}Br_{0.17})_3$	1.63	ITO	1	1.65	18.1	79	23.6	Stanford/ASU/MIT/Oxford [64]	2017
Front planar SHJ	$MAPbI_3$	1.55	IZO	1.43	1.717	16.4	73.1	20.5	EPFL/CSEM [65]	2016
Double side planar SHJ	$MAPbI_3$	1.55	ITO nc-Si	0.12	1.76	14	77	18.1	HZB/EPFL [66]	2016
Double side planar SHJ	$MAPbI_3$	1.55	IZO	0.17	1.69	15.9	79.9	21.2	EPFL/CSEM [67]	2015

Table 2: Summary of the optoelectronic parameters of the 4T perovskite/SHJ TSCs.

Si bottom cell	Perovskite top cell	Eg (eV)	Area (top; bottom) cm^2	V_{OC} (V)	J_{SC} (mA/cm^2)	FF (%)	Eff. (%)	Research institution	Year
Textured SHJ	$Cs_{0.05}FA_{0.81}MA_{0.14}PbI_{2.55}Br_{0.45}$	–	0.049, 0.049	1.12, 0.7	22.3, 17.2	77.7, 76.6	19 + 9.2 = 28.2	UToronto/KAUST [68]	2020
Textured SHJ	$MAPbI_3$	1.55	0.096;1	1.156, 0.698	19.8, 15.6	79.9, 80.1	18.3 + 8.7 = 27	UCAS/SNU [69]	2020
Topcon	$Cs_{0.05}FA_{0.8}MA_{0.15}PbI_{2.55}Br_{0.45}$	1.63	0.059, 0.1	1.1, 0.675	20.6, 16.6	78.9, 79.6	17.8 + 8.9 = 26.7	GT/NREL [70]	2020
Textured SHJ	$MAPbI_3$	1.55	0.16, 4.2	1.008, 0.708	19.8, 18.8	78, 79.3	10.6 + 15.6 = 26.2	KAUST [71]	2019
Textured SHJ + IBC	$CsMAFAPbI_{3-x}Br_x$	1.63	0.36;4	1.1, 0.69	21.5, 14.2	73.5, 81	16.6 + 7.9 = 24.5	ANU/SYSU [72]	2017
Textured SHJ	$MAPbI_3$	1.55	0.25;4	1.069, 0.693	20.1, 15.98	76.1, 79.5	16.4 + 8.8 = 25.2	EPFL/CSEM [65]	2016
Textured SHJ	$MAPbI_3$	1.55	1;4	1.057, 0.692	19.3, 15.5	71.6, 79.4	14.5 + 8.5 = 23.0	EPFL/CSEM [65]	2016
Textured SHJ	MAPbI3	1.55	0.075;4	1.08, 0.679	20.6, 12.3	74.1, 77.9	16.5 + 6.5 = 23.0	UNL/ASU [73]	2016
Textured SHJ	$FA_{0.83}Cs_{0.17}Pb(I_{0.6}Br_{0.4})_3$	1.74	0.09;na	1.10, 0.69	19.9, 13.9	71, 76	12.5 + 7.3 = 19.8	Oxford/HZB [74]	2016
Textured SHJ	$MAPbI_3$	1.55	0.25;4	0.938, 0.693	17.36, 15.81	59.6, 77.4	10.4 + 7.8 = 18.2	EPFL/CSEM [75]	2015
Textured SHJ	$MAPbI_3$	1.55	0.25;4	0.821, 0.689	14.5, 13.7	51.9, 76.7	6.2 + 7.2 = 13.4	EPFL/CSEM/ASCR [76]	2015

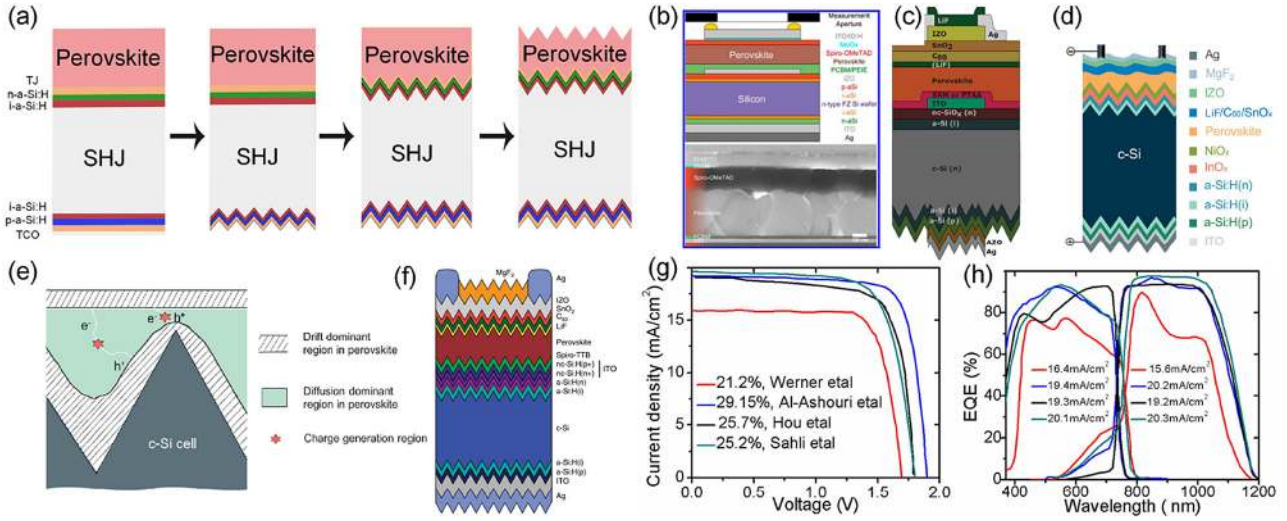

Figure 4: (a) Structure evolution of perovskite/SHJ tandem devices. (b) Cell design of perovskite/ SHJ TSCs with a double side planar SHJ bottom cell [67]. Copyright 2018, American Chemical Society. (c) Schematic view of perovskite/SHJ TSCswith a front planar SHJ bottom cell [52]. Copyright 2020, The American Association for the Advancement of Science. (d) Schematic drawing of perovskite/SHJ TSCs with a textured SHJ bottom cell. Solution-processed micrometer-thick perovskite layer fills the bottom of the pyramid [56]. Copyright 2020, The American Association for the Advancement of Science. (e) Schematic view of electric-field distribution in textured tandem device [56]. Copyright 2020, The American Association for the Advancement of Science. (f) Schematic device design of perovskite/SHJ TSCs with a textured SHJ bottom cell [60]. Conformal perovskite layer is deposited on textured SHJ bottom cell. Copyright 2018, Springer Nature. (g) EQE spectra of perovskite/SHJ tandem cells with different SHJ bottom cells [52, 56, 60, 67]. (h) *J–V* curves of tandem devices with different SHJ bottom cells [52, 56, 60, 67].

To fully harvest the incident photons and reduce costs, double side textured c-Si bottom cell has been used (Figure 4(f)). Sahli et al. used fully textured c-Si bottom cell with random pyramids, resulting in a certified PCE of 25.2% (Figure 4(g)) [60]. The reflection loss was only 1.64 mA · cm^{-2}. A total photocurrent density was 40.4 mA · cm^{-2}, which was close to that of the record Si device (42.5 mA · cm^{-2}) (Figure 4(h)). However, to fabricate conformal and shunt-free perovskite cell, most layers were thermally evaporated in vacuum. Wide-band-gap perovskite materials have mixed cations and mixed halides. This composition requires four or more organic and inorganic precursor sources. Some trace additives, such as KI, PEAI, and $Pb(SCN)_2$, butanethiol, exacerbate the difficulties of control over the deposition rates during the evaporation process [53]. It seems difficult to build up efficient tandems using thermal evaporation. Another approach is to shrink the size of the pyramids and to increase the perovskite charge-carrier diffusion length. Because the thickness of perovskite layer exceeds the height of the pyramid, to be conformal is not required and spin coating can be used. For example, Huang et al. used solution-based blading of perovskites to deposit on the fully textured c-Si bottom cell with pyramids with height less than 1 µm. The tandem device exhibited a PCE of 26.2% with V_{oc}, J_{sc} and FF of 1.82 V, 19.2 mA · cm^{-2} and 75.3% [53]. They found that pyramids with height over 1 µm are not suitable for spin coating method, because perovskite films with 0.5–1 µm thickness cannot completely cover the pyramid. And the thickness of perovskite films is limited by the diffusion length of charge carrier. Meanwhile, pyramids with height of less than 0.43 µm increase the reflectance to 14.2%. Therefore, pyramids with a height ranging from 0.43 to 2.5 µm is a good choice. As shown in Figure 4(d), Hou et al. [56] used spin-coating micrometer-thick perovskites with fully textured SHJ bottom cell, reaching a certified PCE of 25.7% (Figure 4(d)). To improve collection of photogenerated carriers, they increased the depletion width in the perovskites layer [56]. They demonstrated that the depletion region in the perovskite layer at the valley of Si pyramids was wider (380 nm) than at the top (120 nm) (Figure 4(e)). This result indicates that the depletion width increases according to the thickness of perovskite layer, which is useful for charge collection.

The performance of mechanically stacked 4T tandem cells also increased [65, 68–76]. The first report of perovskite/SHJ mechanically stacked tandem cell was published in 2016 by Löper et al. [76], showing a PCE of 13.4%. The latest record was held by Sargent et al. [68] at the UToronto, with a 28.2% PCE obtained from a 4T tandem measurement combining a 0.049 cm^2 perovskite top cell with a SHJ bottom cell. Up to now, most published 4T performance results were based on indirect measurements involving a small perovskite top cell (<1 cm^2) and a lager silicon bottom cell

[65, 68–72, 90]. However, some progress has already been made in upscaling the perovskite top cell. For example, semitransparent modules with a larger aperture area (4 cm^2) have been demonstrated, reaching a PCE of 12%, which resulted in a module-on-cell 4T with 20.2% PCE [91].

4.2 Performance optimization

The performance optimization of perovskite/SHJ TSCs mainly include four aspects: transparent conducting electrode [75, 92–98], electron and hole transport layers (ETLs and HTLs) [99–102], perovskite layer [77–86], and recombination layer [63, 103].

4.2.1 Transparent conducting electrode

In perovskite-based tandems, the top cell should be highly NIR transparent (800–1200 nm) and fully harvest the solar spectrum of blue part (300–800 nm) [71]. Therefore, the front transparent electrode of top cell should avoid parasitic absorption in the blue part of the solar spectrum. The rear transparent electrode of top cell in 4T tandems should minimize the free-carrier absorption in the red part. The losses of parasitic absorption can be reduced by decreasing the free-carrier charge. However, decrease in the carrier charge means bad conductivity for charge collection. A trade-off between the transparency and conductivity against carrier density is observed in these materials. Based on these criteria, transparent conductive oxide (TCO) films have been explored for perovskite-based tandems, which include Sn-doped In_2O_3 (ITO) [52], H-doped In_2O_3(In_2O_3:H) [68], zinc oxide-doped indium oxide (IZO) [50], tungsten-doped indium oxide (IWO) [104], Zr-doped indium oxide (IZRO) [71] and so on. Among this, ITO is commonly used one due to its wide bandgap of 3.5–4.3 eV and high work function of 4.8 eV [33]. Besides, ITO has high available transmittance (above 80%) in visible light and low electrical resistivity (1.5–2.0 × 10^{-4} Ω cm). However, it has high parasitic absorption in NIR range (Figure 5(a)). To reduce resistivity, it requires high deposition temperatures or post annealing to achieve ideal

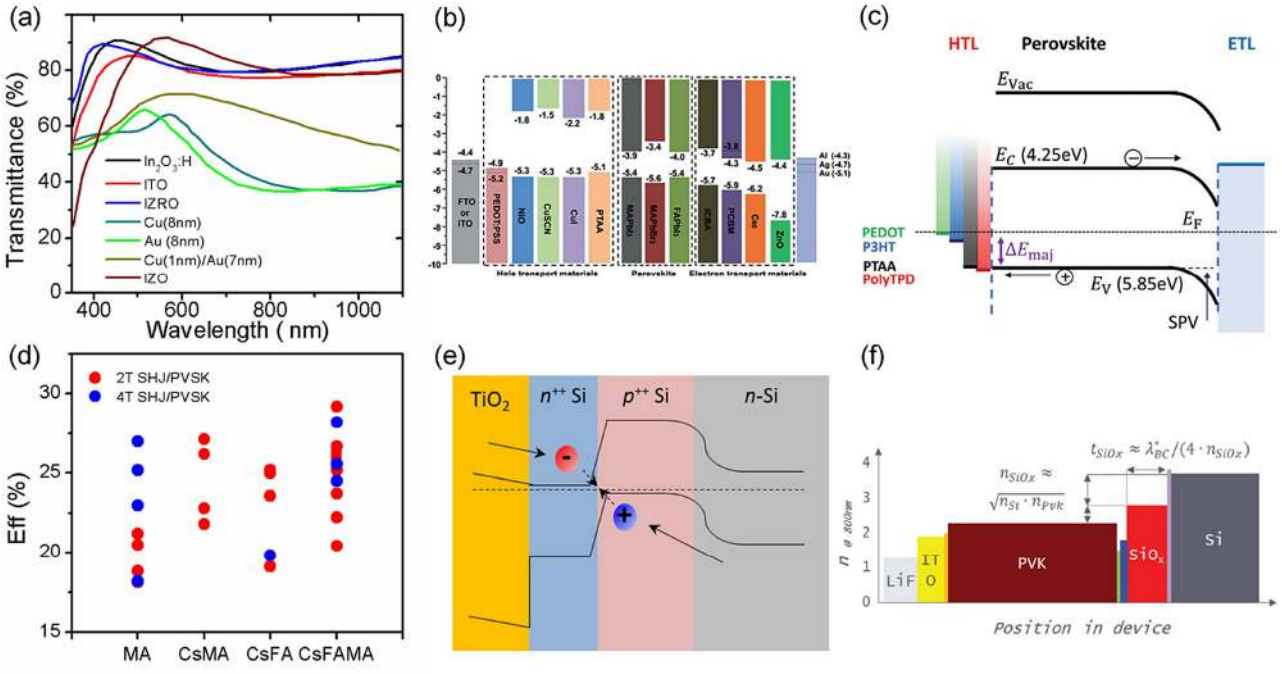

Figure 5: (a) Transmittance (*T*) of different transparent electrodes: In_2O_3:H [68], ITO [68], Zr-doped indium oxide (IZRO) [71], Cu (8 nm) [73], Au (8 nm) [73], Cu (1 nm)/Au (8 nm) [73], and indium zinc oxide (IZO) [75]. (b) Energy level diagram of common materials for *p*–*i*–*n* perovskite solar cells [105]. Copyright 2017, John Wiley and Sons. (c) The energy alignment of perovskite materials and different hole transporting materials. The HOMO of the PTAA and PolyTPD is aligned with the perovskite valence band, which yield high open-circuit voltage. While an internal band gap bending appeared for P3HT and PEDOT: PSS hole transporting materials. This causes the V_{oc} lower than the internal quasi-Fermi level splitting (QFLS) [106]. (d) Comparison of the 2T and 4T tandems efficiency with absorbers containing different cations [107]. (e) Schematic view of perovskite/silicon cell tunnel junction showing the charge-transport mechanism [90]. (f) Schematic of infrared light management using a nanocrystalline silicon oxide interlayer in 2T perovskite/silicon tandem device. The sequence of refractive indices is shown for reference [42]. Copyright 2019, John Wiley and Sons.

crystalline structure. This would degrade the perovskite cell. Magnetron sputtering process can also damage the underlying interface layers and perovskite absorbers. In_2O_3:H has high mobility and optical transparency. But the water vapor effusion would degrade the device performance. Similarly, IZO can be deposited at low temperature and low power, without annealing and the addition of oxygen. Unfortunately, the band edge is blurry, which decreases the transmittance in blue part of spectrum. Besides, IWO can also be used as transparent electric anode, which exhibits 0.6% parasitic absorption in near infrared spectrum. Zheng et al. [104] employed IWO transparent electric anode, yielding average reflectance over 88% in the wavelength range of 750–1100 nm. As shown in Figure 5(a), IZRO has been a good choice due to high NIR transparency and conductivity. Aydin et al. used IZRO to replace the ITO, improving the J_{sc} from 15.6 to 17.4 mA · cm^{-2}, achieving a PCE of 26.2% for 4T perovskite/SHJ solar cell. They demonstrated that the electron mobility could increase to as high as 77 $cm^2 V^{-1} s^{-1}$ and the sheet resistance is only 18 Ω sq^{-1} [71].

Generally, there are two ways to reduce the sputtering damage of TCO: (1) depositing sputter barrier layers [108, 109]; (2) using ultrathin metal electrode instead of TCO. For *n–i–p* cells, thermally evaporated MoO_X is a commonly used sputter barrier layer [109]. Because it interacts with the Ar plasma in the sputter deposition, it shows that parasitic absorption increases with the increase of oxygen vacancies. Other metal oxides, such as NiO_X, VO_X and tungsten oxide (WO_X) can still be suitably used as the sputtering buffer layer. For the *p–i–n* structure, zinc oxide (ZnO) nanoparticles [99, 100] and atomic layer deposited (ALD) SnO_2 [60] layer are used as sputtered buffer layer to avoid bombardment. For example, Bush et al. [64] used a 4 nm ALD SnO_2 and 2 nm zinc tin oxide (ZTO) window layer between the front ITO and LiF/PCBM electron transport layer, yielding a PCE of 23.6% for a 2T tandem device. They found that an SnO_2 layer of 4 nm is necessary to prevent Zn in reaching underneath layers and improve stability for tandems. The only problem of ALD SnO_2 is the effect of water during ALD process [33]. Ultrathin metal electrodes, such as Au, Ag, Al, and Cu have been employed. Huang et al. [73] found that Cu and Au have better stability than Ag and Al under ambient atmosphere. In addition, Cu/Au [73] and MoO_X/Au [96] have also been demonstrated to be transparent conducting electrode with simple manufacturing processes. Yang et al. used MoO_3/Au/MoO_3 sandwiched gold nanomesh as electrode to achieve a PCE of 27.0% for 4T tandem device. The sheet resistance is 19.6 Ω sq^{-1} [69]. However, the average transmission is only 56% in the wavelength range of 800–1100 nm (Figure 5(a)). The major problem for ultrathin metal is strong parasitic absorption in the top cell's sub-bandgap spectral range.

4.2.2 Electron and hole transport layers

The separation and transport capability of free charge carriers are critical for ETLs and HTLs in perovskite/Si tandem device. For efficient tandem devices, HTLs should meet the following criteria: (1) The highest occupied molecular orbital (HOMO) energy or the valence band values should be slightly higher than the valence band of the perovskite layer to improve the hole transfer and electron blocking (Figure 5(b)). (2) High hole mobility is desirable for better transporting [110]. (3) High transparency is required to avoid parasitic absorption. (4) They should be thermally and photochemically stable. (5) They should be processed easily and cost-effective. Generally, HTLs can be divided into three categories: polymeric, small organic molecule, and inorganic. The widely used small molecule for HTL, Spiro-OMeTAD shows strong parasitic absorption in the blue and UV spectral region. Another drawback of Spiro-OMeTAD is high thermal degradation rate. Therefore, polymeric poly(bis(4-phenyl) (2,4-bimethylphenyl) amine) (PTAA) has been used instead of Spiro-OMeTAD. For example, Huang et al. used PTAA with a thickness of 15 nm as HTL to achieve a PCE of 26.2% for 2T tandem device. The spin coated PTAA is thin, uniform and conformal on the pyramids of SHJ bottom cell [53]. Saliba et al. demonstrated that PTAA has a better stability than Spiro-OMeTAD at 85 °C. However, the HOMO energy value of PTAA is about −5.1 eV, which is mismatched to the valance band maximums of perovskite with a range of −5.43 to −5.71 eV [111]. Stolterfoht found that PolyTPD has better HOMO energy value to improve the V_{oc} of SHJ-TSCs (Figure 5(c)). Other polymeric HTLs, P3HT, and PEDOT:PSS also have drawbacks, such as complex purification process, tricky characterization with broad molar mass distribution, and poor batch-to-batch reproducibility [102]. Therefore, many groups have manufactured alternative HTLs with high hole mobility and low cost, such as inorganic NiO, CuI, and CuSCN [102]. NiO is a wide band gap HTL that has been exploited successfully in perovskite/SHJ TSCs. Xu et al. [52] used NiO_x/polyTPD bilayer HTLs to achieve a V_{oc} of 1.886 V for 2T tandem device. They demonstrated that 20-nm-thick sputtered NiO_x could reduce the shunting. However, the photostability of NiO_x based TSCs is poorly explored [112].

For efficient perovskite cells, the ETLs extract the electrons from the perovskite layer to the cathode. Therefore, good energy-level alignment and high electron mobility are essential to guarantee the electron transport.

The deeper valence band edge (VB) is needed to block injection of holes. High transmittance can reduce the parasitic absorption losses. Besides, the stability and cost also influence the application of ETLs [113]. There are several different types of ETLs include TiO_2, SnO_2, ZnO, phenyl-C61-butyric acid methyl ester (PCBM), and C60. Historically, a TiO_2 mesoporous scaffold layer was firstly used as ETL with a sintering step at 500 °C in perovskite solar cell [75]. However, this relatively high temperature is not suitable for c-Si/a-Si heterojunction bottom cell. ZnO owns high electron mobility of 205–300 $cm^2\ V^{-1}\ s^{-1}$ and low temperature process. But it will react with perovskite when the annealing temperature exceeds 100 °C [100]. As shown in Figure 5(b), SnO_2 owns deep valence band level with a range of −4.2 to 4.5 eV and high electron mobility of 240 $cm^2\ V^{-1}\ s^{-1}$. However, the solution processing of SnO_2 would dissolve the already deposited perovskite layer for pin perovskite/SHJ TSC. Therefore, SnO_2 buffer layer is commonly prepared by low temperature ALD. SnO_2 also has some drawbacks such as interface recombination and inefficient electron extraction [113]. Therefore, fullerene (C_{60}) and its derivatives such as PCBM were used to passivate the perovskite surface defects and suppress hysteresis [114]. Xu et al. [52] used C_{60}/bathocuproine (BCP) as ETLs to achieve a PCE of 27.13% for 2T perovskite/SHJ TSC. Because the parasitic absorption of C60, the current density is only 19.12 $mA{\cdot}cm^{-2}$. The morphology control and frontier orbital position also need to be optimized to enhance the performance.

4.2.3 Perovskite absorption layer

At first, $MAPbI_3$ was used as top cell for perovskite/SHJ TSCs. However, the band gap of $MAPbI_3$ is about 1.55–1.63 eV, which is below the optimize range of 1.67–1.75 eV [33]. The band gap of $MAPbI_3$ can be increased by replacing part of iodine with bromine at the halogen anion site X. Unfortunately, wide band gap perovskite with high Br content is limited by photoinduced phase segregation [115]. Under illumination, the perovskite decomposes into Br- and I-rich regions. The I-rich regions own narrow band gap, and act as gap defect or trap states. Light induced phase segregation leads to significant V_{oc} loss for perovskite cells, so wide band gap perovskite solar cell exhibits larger V_{oc} deficit ($Eg/q - V_{oc}$) than narrow phase.

As shown in Figure 5(d), mixed cations of FA, Cs, and MA at A-site is the best choice for the perovskite absorption layer. The mixed cations of FA, Cs, or Rb can reduce phase segregation and improve material quality [61]. However, the FA/Cs based perovskite film has small grains, which leads to high density of grain boundaries and high surface recombination [37]. Therefore, several approaches have been proposed, such as increasing grain size, surface passivation, 2D/3D heterojunction engineering, and ion compensation [116]. For example, Al–Ashouri et al. [50] used a composition of $Cs_{0.05}(FA_{0.77}MA_{0.23})0.{}_{95}Pb(I_{0.77}Br_{0.23})_3$ and obtained a PCE of 29.15% and a maximum V_{oc} of 1.9 V in 2T perovskite/SHJ TSC. Performance improvements in wide band gap perovskite solar cell was made by increasing the Cl content in lattice and replacing I partially with Br [52]. Huang et al. used a $Cs_{0.15}(FA_{0.83}MA_{0.17})_{0.85}Pb(I_{0.7}Br_{0.3})_3$ perovskite top cell with band gap of 1.70 eV and achieved a PCE of 25.4% for 2T perovskite/SHJ TSC [58]. They found that the addition of MACl could increase the grain size, while the addition of MAH_2PO_2 could reduce nonradiative recombination by passivation of grain boundary [58]. Kim et al. [54] used 2D/3D mixed wide band gap perovskite-$(FA_{0.65}MA_{0.2}Cs_{0.15})Pb(I_{0.8}Br_{0.2})_3$-as top cell, and obtained a PCE of 26.7% for 2T perovskite/SHJ TSC. PEA-based additives have been proven to be critical to form the 2D passivation layer and improve the V_{oc} and FF. Sargent et al. used a Lewis base as additive to reduce the trap density and increase the electron-diffusion length, yielding a PCE of 19% for semitransparent perovskite top cell. By combining this perovskite cell with a textured SHJ cell, the best PCE of 4T tandem device is 28.2% [68].

4.2.4 Recombination layer

For high efficiency TSCs, the tunnel junction should meet the following standards: (1) minimal resistive losses and maximal optical transparency; (2) a barrier to prevent the solvent and ions from penetrating into bottom cell; (3) poor in-plane conductivity and good out-plane conductivity to reduce shunts; and (4) compatible with the above and underneath layer fabrication processes. As shown in Figure 5(e), the first tunnel junction of 2T TSC was based on crystallized p^{++}-Si/n^{++}-Si recombination layer. In essence, the quasi-Fermi level (E_F) on both side of the p–n-junction transfers to the valence (E_V) and conduction (E_C) band due to the high doping levels. Once a positive voltage is applied to the p–n-junction, full states of the n-side align with empty states of the p-side. To activate the dopants, the a-Si:H layer was annealed at 680 °C for 15 min [90]. This high temperature is not suitable for the c-Si/a-Si heterojunction bottom cell. To address this issue, TCO-based tunnel junctions have been fabricated by low-temperature process such as ITO, IZO, and ZTO. For example, Albrecht et al. used 20 nm ITO layer as tunnel junction and achieved a certified PCE of 25% for 2T perovskite/SHJ TSC [55]. The EQE current density of perovskite and c-Si were 20.69 and 17.85 $mA \cdot cm^{-2}$, respectively, indicating that the current

was limited by the bottom cell of c-Si, which was mainly due to the refractive index mismatch between ITO and its adjacent layers. To address this issue, Mazzarella et al. employed nanocrystalline silicon oxide (nc-SiOx:H) interlayer under the ITO, resulting in 1.4 mA · cm^{-2} J_{sc} gain in the bottom cell. As shown in Figure 5(f), the 110 nm thick nc-SiO_x:H with refractive index of 2.6 (at 800 nm) was the best choice for infrared light management [42]. At present, the lowest electrical resistivity of ITO is 1.5×10^{-4} Ω cm. However, the lateral conductivity and longitudinal conductivity of ITO are the same, which leads to shunt paths for top cell. Therefore, nc-Si:H tunnel junction was fabricated to replace ITO. The *Eg* of nc-Si:H is narrower than that of ITO, so it only absorbs the blue region of the spectrum that the top cell has absorbed. Besides, the high-density grain boundary of nc-Si:H impedes the lateral transport of charge carriers. The large single grains span across the tunnel junction to improve the longitudinal conductivity. By implementing nc-Si:H tunnel junction in a 2T tandem device, Sahli et al. obtained a PCE of 25.2%. The EQE current density of the tandem device was improved to 19.5 mA · cm^{-2}. This work represents a key step toward controlled fabrication of efficient large area perovskite/SHJ TSCsusing the knowledge of nc-Si:H recombination layer.

4.3 Toward market

For market application, perovskite/SHJ TSCs are facing several challenges such as long-term stability, device area upscaling, and material toxicity [117]. The stability of perovskite solar cells depends on the surrounding environment including humidity [118, 119], oxygen [120], temperature [121, 122], and light illumination [81, 120, 123]. The halogen ions at X-site influence the photoinstability of wide band gap perovskite solar cells. As discussed before, using partial Cl to replace I could improve the photostability of perovskite material [52]. The instability of moisture and oxygen is closely related to the A-site cation. Cs-doped mixed-cation perovskite shows long time stability under heat stress and humidity environments [107]. For example, Xu et al. [52] used $Cs_{0.75}MA_{0.22}Pb(I_{0.82}Br_{0.15}Cl_{0.03})_3$ perovskite top cell to achieve less than 4% degradation after 1000 h of operation at 60 °C under 100-sun illumination. Further stability improvement can be seen through appropriate glass/polymer encapsulation. Encapsulating with glass and butyl rubber, Hou et al. [56] demonstrated that the TSCs retained their original performance at 85 °C for 400 h in the dark.

At present, the fabrication of large area perovskite/SHJ TSCs (>1 cm^2) and modules (>10 cm^2) faces many challenges, such as fabrication method, film quality, and long-time stability. Due to poor uniformity and material waste, spin-coating is not suitable for upscaling perovskite/SHJ TSCs. Large area deposition methods have been presented such as inkjet printing, blade coating, spray coating, slot-die coating. However, commercial c-Si cells are textured, which hinders the use of solution methods. Therefore, vapor deposition has been developed to make uniform large area perovskite TSCs [26]. First demonstration of large area perovskite/SHJ TSC was presented by Sahli et al. [63], with 18% PCE of 12.96 cm^2. Encouragingly, Oxford PV obtained a PCE of 28% for 2T perovskite/SHJ TSC (1 cm^2) by a vapour deposition. This device has been passed the 2000 h damp heat reliability test (IEC 61215). To achieve the commercial application of perovskite/SHJ TSCs, it is necessary to put more effort into large area cells while maintaining the high PCE.

Lead toxicity is another issue related to the photovoltaic application of perovskite materials. To this end, several groups have demonstrated the ability to fabricate lead-free, or lead-less perovskite solar cells [124]. However, the PCE of these devices are much lower than that of current lead-containing devices. In addition, environmentally friendly solvents should be considered to replace toxic solvents such as dimethylformamide and dimethyl sulfoxide. It is no exaggeration to say that the research to put perovskite/SHJ solar cells into practical application is still at a rudimentary stage.

4.4 PCE prospect and improvement strategy

Currently, 2T perovskite/SHJ TSCs have reached a high PCE of 29.5%, and further improvement strategy should be proposed. The record-efficiency top cell parameters are shown in Figure 6(a)–(d) for 2T and 4T SHJ tandem devices. Compared to GaInP top cell, the main limitations of wide band gap perovskite cells are V_{oc} and FF. A minimum V_{oc} deficit of perovskite top cell is 0.45 V [52], which is far below than the optimum 0.34 V [125]. It is noticed that the V_{oc} deficit of GaInP (1.81 eV) cell is only 0.32 V (Figure 6(b)). This indicates that there is large potential for improving the V_{oc} of perovskite/SHJ TSCs. By passivating defects to reduce nonradiative recombination, the V_{oc} of 1.67 V of the perovskite top cell can be enhanced to 1.35 V, while the V_{oc} of SHJ cell can be increased to 0.75 V by reducing the thickness of Si wafer. The total V_{oc} can be increased to 2.08 V for 2T perovskite/SHJ TSCs. Currently, the record FF of 2T perovskite/SHJ TSC is only 79.9%, which is much lower than the 89.8% of 2T III–V/Si TSC (Figure 6(d)) [126]. A main FF limitation of perovskite solar cells is the ideality

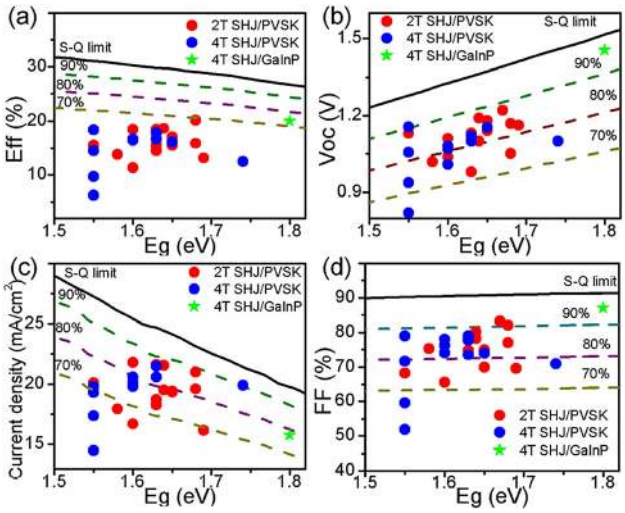

Figure 6: Record-efficiency top cell parameters as a function of band gap for 2T and 4T SHJ tandem devices. The red and blue spheres represent the record-efficiency cell parameters for 2T and 4T SHJ/perovskite tandems respectively (see Tables 1–2 for references). The green star shows record-efficiency GaInP cell parameters for 4T SHJ/GaInP TSC [23]. The black line represents SQ limit for single junction solar cell. The green, violet and light green dashed lines represent 90, 80 and 70% SQ limit for single junction solar cell respectively.
(a) Power-conversion efficiency (PCE). (b) Open-circuit voltage (V_{oc}). (c) Short-circuit current (J_{sc}) and (d) Fill factor (FF). All data are for standard AM1.5 illumination at 1000 W/m^2.

factor (n) [50]. The optimal value of the ideality factor is about 1–1.3. However, the high efficiency perovskite solar cells exhibit high values of 1.4 to 1.8. Therefore, it is essential to reduce the ideality factor by minimizing nonradiative recombination. Noticing that point defect such as organic cation vacancies and halide anion vacancies in grain boundaries is closely tied to the nonradiative recombination [35]. Thus, charged components compensation by quaternary ammonium and halide ions may be a good choice to reduce nonradiative recombination. In addition, the contact resistance between the transparent electrode and the grid also limits the FF. Therefore, reducing contact resistance and improving carrier extraction are beneficial to obtain the ideal FF. The theoretical J_{sc} can reach to 22 mA $\cdot$ cm^{-2} for perovskite top cell with a band gap of 1.75 eV [127]. Up to now, the record J_{sc} of perovskite/SHJ TSCs is 19.22 mA $\cdot$ cm^{-2}, while the record J_{sc} of semi-transparent perovskite top cell is 19.6 mA $\cdot$ cm^{-2} with a band gap of 1.68 eV (Figure 6(c)) [128]. By depositing conformal perovskite layer on textured Si cell, the J_{sc} is predicted to achieve 20 mA $\cdot$ cm^{-2} [60]. By these optimizations, a tandem efficiency of 35% could be expected a V_{oc} of 2.08 V, a J_{SC} of 20 mA $\cdot$ cm^{-2} and an FF of 85%. Then the PCE reaches the 77% of their SQ-limit of 45.7% (Figure 6(a)).

5 III–V/SHJ TSCs

Compared with perovskite materials, III–V compound semiconductor materials, with their excellent proven reliability and adjustable band gap, exhibit high efficiency and promising potential for industrial application. In many cases, III–V semiconductor multijunction solar cells are superior to other solar cells. However, the high costs preclude their use for nonconcentrator terrestrial application. To address this issue, III–V/SHJ TSCs have appeared on the road map of many PV companies. At present, many strategies have been used to fabrication III–V/SHJ TSCs, including heteroepitaxial growth, wafer bonding and mechanical stacking. The purpose of this section is to summarize all these studies, with an emphasis on examples demonstrated by wafer bonding.

5.1 Heteroepitaxial growth

Heteroepitaxial integration approach is probably the earliest explored approach towards the fabrication of III–V/Si TSCs such as AlGaAs/Si [129], GaAsP/Si [130]. In principle, it is possible to fabricate high efficiency III–V/Si tandem devices by controlling the density of threading dislocations. The growth of a polar III–V compound semiconductor on nonpolar Si would create defects such as antiphase domains (APDs). These APDs can be effectively removed by using a (100) Si wafer with a 4°–6° offcut in the (111) direction [131]. Another obstacle is the 4% lattice-mismatch between GaAs (αGaAs = 0.56 nm) and Si (αSi = 0.54 nm), which can lead to threading dislocations and misfit dislocations (Figure 7(a)). Two possible approaches have been proposed, one is the thermal-cycle annealing (TCA), and the other is low growth rate and low temperature process during the primal GaAs nucleation on Si. For instance, Akiyama et al. [21] have demonstrated that GaAs layer can be directly grown on (100) Si substrates without buffer layers. Firstly, the 10 nm thick GaAs layer was deposited at 400 °C to enhance the nucleation. Then, the temperature was increased to 650–700 °C to obtain a better and uniform epitaxial layer. Yamaguchi et al. found that TCA could effectively increase the dislocations movement and reduce the stress in the crystal, thus reducing dislocation densities. The difference of thermal expansion coefficients between GaAs (5.73×10^{-6} °C^{-1}) and Si (2.6×10^{-6} °C^{-1}) lead to residual strain in the material, which will result in poor crystalline quality. Inserting buffer layers between the III–V material and the Si substrate is a promising approach to limit the impact of crystal defects. Optical transmissivity, electrical conductivity, and

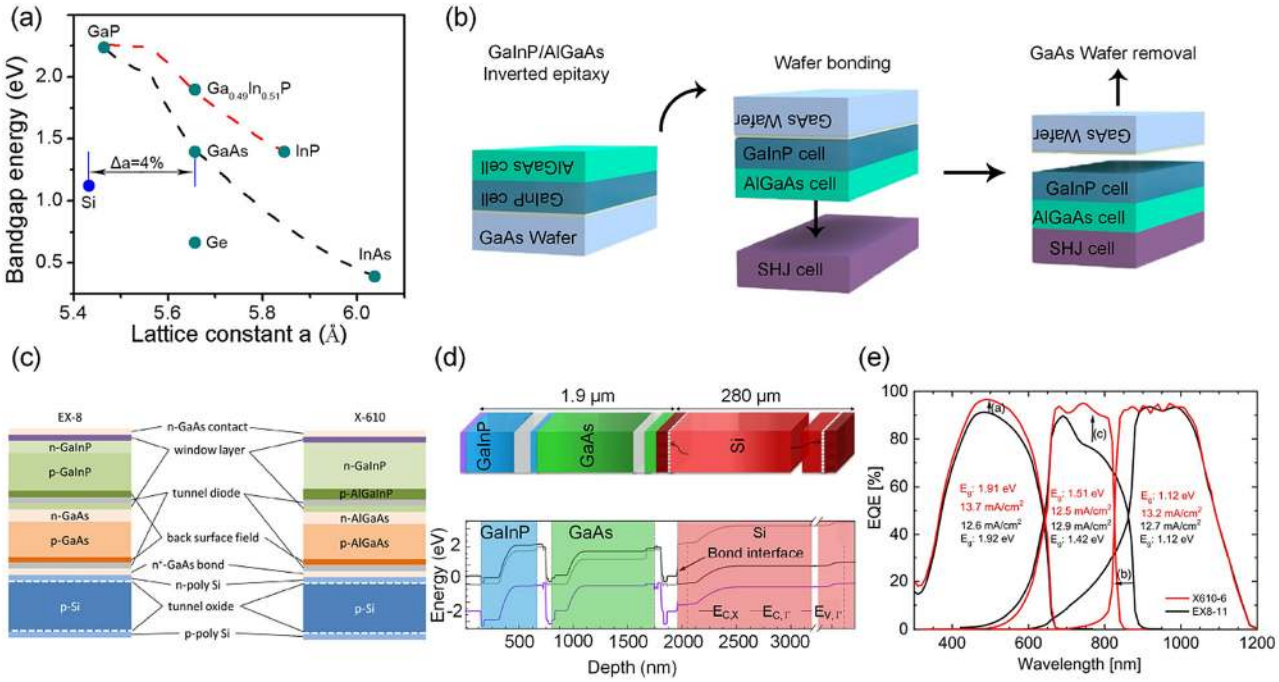

Figure 7: (a) Bandgap energy as a function of lattice constant for silicon, germanium and III–V semiconductors. Different strategies to overcome the difference of 4% lattice constant between GaAs and Si [36]. Copyright 2018, Elsevier. (b) Typical wafer bonding process of a 2T GaInP/AlGaAs/Si triple junction tandem device [132]. (c) The comparison of inverted grown EX-8 and "upright grown" X-610 GaInP/AlGaAs(GaAs)/Si triple junction solar cells [47]. Copyright 2020, John Wiley and Sons. (d) Layer stack and band structure of a 2T $Ga_{0.51}In_{0.49}P$/GaAs/Si solar cell [45]. $E_{V,\Gamma}$ (purple line), $E_{C,\Gamma}$ (direct transition, grey line), and $E_{C,x}$ (indirect transition, black line) are shown in band structure under open-circuit condition without illumination [45]. Copyright 2018, Springer Nature. (e) Measured EQE spectra of inverted grown EX-8 and "upright grown" X-610 GaInP/AlGaAs(GaAs)/Si triple junction solar cells [47]. Copyright 2020, John Wiley and Sons.

thickness are three important parameters of the buffer layer. Currently, common buffer layers include SiGe [133], GaAsP [134], AlGaAs [135], and GaAs [136]. Compared to low-bandgap SiGe buffers and wide bandgap GaAsP would be a better choice to minimize the dislocation [136]. However, the decrease of threading dislocations density to 10^7 cm^{-2} is still deleterious for minority carrier devices, so this approach remains challenging.

So far, the highest reported AM1.5G efficiency of 22.3% is achieved by Feifel and coworkers [137] for a GaInP/GaAs/Si TSC in 2019. The 200 nm thick $GaN_{0.024}P_{0.976}$ deposited on the GaP nucleation layer to reduce defect density at the GaP/Si interface. Then, the temperature was increased to 700 °C during the $GaAs_yP_{1-y}$ buffer growth. Due to the high temperature, silicon bottom solar cells are mainly silicon homojunction solar cells. Due to stable and high PCE, it is expected that new SHJ solar cells will replace silicon homojunction solar cells.

5.2 Wafer bonding

Wafer bonding approach seems to be the most successful approach for fabricating high-performance tandem device with relatively larger size. Compared with heteroepitaxial, wafer bonding is not limited by the lattice matching and thermal expansion coefficients. The defect network required for lattice mismatch is confined at bonded interfaces [126]. This process was originally developed by Lasky in 1985s, and reexamined by Cariou, Shigekawa, and many other research groups to fabricate Si/Si [138] Ge/Ge [139], Si/GaAs [45], AlGaAs-Si [140], Si/InP [136], and Si/InGaP [136] junctions. A typical wafer bonding process starts with wafer preprocessing by a chemical solution or plasma, followed by mechanical compression, and ends with postannealing of wafers to form strong bonds. The wafer bonding is mainly induced and dictated by hydrogen bridge bonds or van der Waals interactions, which are two orders of magnitude weaker than covalent bonds. In this sense, the electrically conductive bond layers should have very low surface roughness (<0.2 nm) and must be free from void [132]. As a major requirement, there should be a good chemical mechanical polishing step capable of forming two mirror surfaces, ideally they should be able to form compact bonding layer with higher bonding energy.

At present, wet-chemical etching and surface activated bonding (SAB) are two main methods of wafer bonding. For the former, a hydrogen-terminated surface is

generated by wet-chemical etching. After compression, two hydrophobic surfaces are connected by weak hydrogen-bridge bonds [141]. Finally, hydrogen is desorbed to form covalent bonds at the interface by post-annealing (>800 °C). Another technique is the SAB in which the surfaces are activated by plasma or a fast argon atom or highly energetic ion-beam [142]. Post-annealing is not required because it lowers the bonding energy. All major steps involved in a SAB process are schematically illustrated in Figure 7(b), with the fabrication of GaInP/GaAs/Si TSCs as an example. Based on the schematic diagram of GaInP/GaAs/Si tandem device, Si, and GaAs wafers formed tandem structure when they were loaded on top and bottom electrodes into a bond chamber [132]. An argon fast atom beam was employed to remove the surface oxide, and no re oxidation occurred in the bonding layer under high vacuum ambient ($<3 \times 10^{-8}$ mbar). The wafers were brought in contact under the force of 10 kN for a few minutes. The GaAs growth substrate was then etched away by H_2O_2 and NH_4OH solution. In order to obtain a good bonding mechanical quality, nearly perfect surface must be bonded together with low surface roughness and small particle pollution. Cariou et al. [45] have demonstrated a 2T GaInP/GaAs//Si solar cell with AlGaAs/GaAs tunnel junction reaching a notable PCE of 33.3% (1-sun, AM1.5G) (Figure 7(d)). Due to a diffractive crossed grating made of a polymeric resist at the rear side of TOPcon bottom cell, internal light trapping was enhanced and the device was close to current matching (Figure 7(e)) [45]. Furthermore, Lackner et al. [47] used $Ga_{0.51}In_{0.49}P/Al_{0.06}Ga_{0.94}As$ (1.91eV/1.51eV) top cell to replace the former GaInP/GaAs (1.92/1.42 eV), yielding an increase in 50 mV for V_{oc} and 2.6% for FF (Figure 7(c)).

One of the challenges faced by SAB is to select the appropriate tunnel junction [143]. As shown in Figure 8(a), there are two types of tunneling mechanisms in the tunnel junction: direct transition (band to band) and trap assisted tunneling (TAT). Direct transition even takes place in intrinsic materials where no trap exists. According to quantum mechanical principles, if energy and momentum are conserved, charge carriers can pass through potential barriers. However, after reaching the characteristic peak of tunnel current density, the current drops sharply (Figure 8(b)). This property can be attributed to occupied states of the *n*-side which are aligned longer with empty

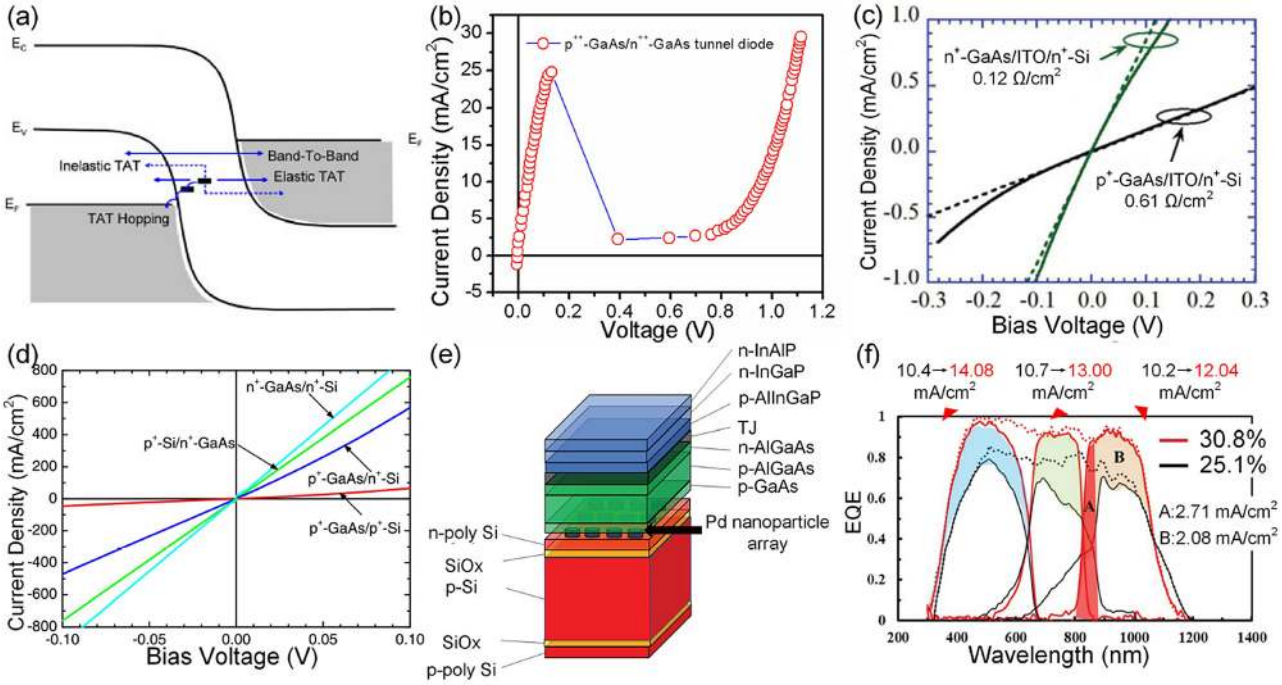

Figure 8: (a) Schematic view of the different tunneling mechanisms in a tunnel diode, (TAT = trap assisted tunneling) [144]. Copyright 2008, John Wiley and Sons. (b) Measured IV curve of p^{++}-GaAs/n^{++}-GaAs tunnel junction [144]. Copyright 2008, John Wiley and Sons. (c) Measured *I*–*V* curve of a n^+-GaAs/ITO/n^+-Si and p^+-GaAs/ITO/n^+-Si 2T tandem devices with a postanneling (400 °C for 5 min) [137]. (d) *I*–*V* characteristics of p^+-Si/n^+-GaAs, p^+-GaAs/p^+-Si, n^+-GaAs/n^+-Si and p^+-GaAs/n^+-Si tunnel junctions measured at room temperature [137]. (e) Schematic diagram of a 2T InGaP/GaAs/Si TSC with Pd nanoparticle arrays as bonding mediators [46]. Copyright 2019, John Wiley and Sons. (f) EQE spectra of InGaP/GaAs/Si and InGaP/AlGaAs/Si TSCs with Pd nanoparticle arrays as bonding mediators [46]. Copyright 2019, John Wiley and Sons.

states on the p-side. Similar to buffer layer, optical transmissivity, electrical conductivity, and thickness are three key parameters of tunnel junctions. The AlGaAs/GaAs tunnel junction is widely used in III–V/Si TSC. The major advantage of AlGaAs/GaAs tunnel junction is that AlGaAs could be more easily doped with carbon than GaAs. Besides, a high aluminum content layer has a diffusion suppressing effect [145]. In contrast, GaAs/GaAs tunnel junction is limited by the optical absorption due to the Moss Burstein effect of *p*-type layer [143]. AlGaAs/GaInP tunnel junction is more difficult to fabricate due to tellurium segregation on the growing surface during high doping [146].

Another challenge faced by SAB is to select the appropriate heterointerface to form an ideal interface resistance also. So far, different heterointerfaces have been extensively studied, such as p^+-GaAs/p^+-Si [147], p^+-GaAs/n^+-Si [148], n^+-GaAs/n^+-Si [149]. For instance, Liang et al. have demonstrated that the interface resistances of p^+-GaAs/n^+-Si, p^+-GaAs/p^+-Si, n^+-GaAs/n^+ Si, n^+-GaAs/p^+-Si were 0.196, 1.887, 0.112 and 0.132 Ω cm^2, respectively (Figure 8(d)) [148]. In essence, different polarity and doping concentration play an important role in the value of interfacial resistances. Using this information, one can obtain ideal interface resistances as small as a few milliohms by optimizing the thickness and doping concentration in the proper ranges. For example, Essig et al. proved that the lowest interface resistance of *n*-Si and *n*-GaAs could be reduced to 2.5×10^{-3} Ω·cm^2 by adjusting the carrier concentration at the surface. However, fast atom beam (FAB) can cause damage to the surfaces of bonded substrates. Shigekawa et al. [142] attempted to insert an ITO layer between Si and GaAs to reduce the damage. They found that the interface resistances of p^+-GaAs/ITO/n^+-Si and n^+-GaAs/ITO/n^+-Si were 0.61 and 0.12 Ω·cm^2 (Figure 8(c)), respectively. The difference of the interface resistances was likely due to a potential barrier generated by the midgap states at the bonding interfaces. Noting that InGaP/GaAs/Si triple-junction (3J) solar cells with an n^+-GaAs/ITO/n^+-Si showed an efficiency of 18% with a V_{oc} of 2.69 V, a J_{SC} of 10.6 mA · cm^{-2} and an FF of 84.1%.

5.3 Mechanical stacking

Mechanical stacking integration represents a straightforward route to III–V/Si tandem device. In this approach, a glass slide with an III–V top cell is attached to the bottom cell SHJ solar cell with a transparent and insulating adhesive. Epoxy has been successfully demonstrated by several groups, with notable examples including 4T GaInP/GaAs/Si [49], GaAs/Si [23], and GaInP/Si [150, 151] tandem devices. It is generally accepted that mechanical stacking provides a simple, high-performance procedure that also allows the variety of top-cell materials present on the silicon bottom cell, to be stacked in a single step. For example, Essig et al. [150] fabricated mechanically stacked 4T GaInP/Si tandem device using a transparent epoxy between the subcells. A PCE of 27.08% is achieved by optimizing the long-wavelength light and luminescent coupling between the two junctions. Moreover, Essig et al. [23] have demonstrated that by mechanical stacking GaInP/GaAs top cell on SHJ bottom cells, the PCE of tandem device could reach to 35.9%.

Tables 3 and 4 show the evolution of the 2T and 4T III–V/Si TSCs technology efficiency, respectively. In addition to insulating adhesive, metal, and metal nanoparticle can serve as a class of transparent conductive adhesive for fabricating III–V/Si tandem device [154]. In this regard, Pd nanoparticle array that could be conveniently patterned on the top of silicon bottom cell using a selfassembled template of polystyrene-block-poly(2-vinylpyridine) (PS-b-P2VP) to fabricate tandem device (Figure 8(e)) [149]. Synthesis of these nanoparticle arrays with different materials, for instance, provides a powerful route to the fabrication of III–V/Si tandem device from various subcells. As shown by Mizuno et al. [149], Pd nanoparticle array as thin as 37 nm could be prepared by copolymer-templated fabrication. This leaded to a Pd nanoparticle density of 60 ng/cm^2 and surface coverage ratio of 12%. The 3J InGaP/GaAs//Si tandem device with a Pd nanoparticle array showed a PCE of 25.1% with a V_{oc} of 2.88 V, a J_{SC} of 10.51 mA·cm^{-2} and an FF of 83% [149]. Moreover, Makita et al. used InGaP/AlGaAs two junction cell and TOPCon bottom cell to replace the former InGaP/GaAs top cell and Al-BSF Si bottom cell, improving the J_{sc} from 10.51 to 12.72 mA·cm^{-2}, resulting in a PCE of 30.3% for 2T III–V/Si TSC (Figure 8(f)). By using $Al_{0.06}Ga_{0.94}As$ (1.50 eV) middle cell, the absorption edge decreased from 870 to 830 nm. Therefore, the current density of Si bottom cell increased by 2.71 mA·cm^{-2}.

6 Conclusion and outlook

This review provides an overview on different methods that have been developed for fabricating TSCs. We briefly discussed a series of methods for fabricating TSCs that are based on the upscaling of small area solar cells, with an emphasis on perovskite/SHJ and III–V/SHJ tandem device. The big challenge for perovskite/SHJ TSCs is the V_{oc} loss. The main reason is nonradiative recombination at the grain boundary and interface. To address this issue, a range of

Table 3: Summary of the optoelectronic parameters of the 2T III–V/Si TSCs.

Si bottom cell	Top cell	Area (cm^2)	V_{OC} (V)	J_{sc}(mA/cm^2)	FF (%)	Eff (%)	Research institution	Year
TOPCon	GaInP/AlGaAs	3.984	3.177	12.4	86.4	34.1	Fhg-ISE [47]	2020
TOPCon	GaInP/AlGaAs	0.09538/0.16	3.03	12.72	80	30.8	AIST [46]	2019
POLO-IBC	GaInP	0.567	2.035	14.9	86.2	26.4	NREL [32]	2019
c-Si	GaInP/GaAs	–	2.619	10	85	22.3	Fhg-ISE [137]	2019
TOPCon	GaInP/GaAs	3.984	3.127	13.7	80.1	33.3	Fhg-ISE [45]	2018
c-Si	Al0.2Ga0.8As	–	1.63	15.16	82.5	21.1	CEA- [152]	2018
c-Si	GaInP/GaAs	4	2.32	10	84.3	19.7	Fhg-ISE [153]	2018
c-Si	InGaP/GaAs/GaAs	0.25	3.29	7.4	76	18.5	AIST [154]	2018
c-Si	GaInP/GaAs	0.04	2.69	10.6	84.1	18	OCU [142]	2018
c-Si	AlGaAs	–	1.63	11.9	65	12.7	UWM [140]	2018
c-Si	GaInP/GaAs	3.963	3.046	11.9	83	30.2	Fhg-ISE [132]	2017
c-Si	GaInP/AlGaAs	4	2.902	10	89.8	26.2	Fhg-ISE [126]	2017
c-Si	GaInP/GaAs	0.11284	2.88	10.51	83	25.1	AIST [149]	2017
c-Si	InGaP/GaAs	0.1448	2.81	10.46	79	23.2	AIST [155]	2016
c-Si	InGaP/GaAs	0.25	2.847	10.94	81.83	25.5	OCU [156]	2015
c-Si	GaInP/GaAs	0.049	2.877	10.1	87.1	25.2	Fhg-ISE [157]	2015
c-Si	GaInP/GaAs	4.003	2.39	12.7	85.9	26	Fhg-ISE	2014
c-Si	InGaP/GaAs	0.04	2.66	10.9	84.2	24.4	OCU [158]	2014
c-Si	GaInP/GaAs	4	2.45	11.2	75.3	16.4	Fhg-ISE [159]	2014
c-Si	GaInP/GaAs	0.055	2.78	8.56	86.3	20.5	Fhg-ISE [160]	2013
c-Si	Al0.1Ga0.9As	1	1.55	27.9	58	25.2	UTokyo [161]	2012
c-Si	AlGaAs	–	1.57	23.6	77.2	21.2	NZT- [162]	1997

Table 4: Summary of the optoelectronic parameters of the 4T III–V/Si TSCs.

Si bottom cell	Top cell	Area (cm^2)	V_{oc} (V)	J_{sc} (mA/cm^2)	FF	Efficiency	Research institution	Year
Textured SHJ	GaInP/GaAs	1	2.520, 0.681	13.61, 22.03	87.5, 78.5	30.01 + 5.9 = 35.91	EPFL [23]	2017
POLO-IBC	GaInP/GaAs	1	2.535, 0.67	13.43, 10.4	87.9, 18.8	29.94 + 5.49 = 35.43	ISFH [49]	2017
Textured SHJ	GaAs	1	1.092, 0.683	28.9, 11.07	85.0, 79.2	26.83 + 5.99 = 32.82	EPFL [23]	2017
POLO-IBC	GaInP	1	1.43, 0.3687	15.4, 24.2	86.6, 75.1	19.1 + 12.5 = 31.5	ISFH [49]	2017
Textured SHJ	GaInP	1	1.456, 0.667	14.15, 22.7	87.9, 76.2	18.1 + 11.7 = 29.8	NREL [151]	2016
TOPcon	GaInP	1	1.444, 0.605	14.6, 23.3	87.9, 60.5	18.54 + 8.54 = 27.08	NREL [150]	2015

strategies have been applied including increasing grain size, surface passivation, heterojunction engineering, and ion compensation. Defects passivation is the most powerful means to improve V_{oc}. Intense studies are focusing on Lewis bases/acids, alkali metal ions (Na, K, Ru, Cs), ligand passivation, halogen ion (Cl, Br), PbI_2, 2D perovskite, insulating polymers, and guanidinium-based additives. The band alignment of charge transporting layer also plays a key role for V_{oc} improvement. Another issue is fabricating perovskite top cell on textured c-Si cell, vacuum deposition method may be a good option. To further improve the TSCs performance, optical and electron losses should be minimized. If these issues are solved, a PCE over 35% can be expected. For up-scaling fabrication and commercialization, long-term stability and material toxicity are also needed to be optimized.

As for III–V/Si TSCs, heteroepitaxial integration approach based on the control of dislocation densities at the interface are able to produce devices, but in poor quality. So far, approaches based on the SAB seem to be most versatile in fabricating high efficiency III–V/SHJ TSCs. This method, however, is not appropriate for using with textured SHJ solar cells, and the requirement of clean room environment and tunnel junction may also cause high cost. Therefore, mechanical stacking by transparent conductive adhesive and metal nanoparticle array may be a new research direction for high performance III–V/SHJ TSCs. Judged against high performance and low cost, all the approaches described in this review need to be improved before they can be widely used in commercial applications.

Author contributions: All the authors have accepted responsibility for the entire content of this submitted manuscript and approved submission.

Research funding: The authors gratefully acknowledge the supports from National Key Research and Development

Program of China (Grant No. 2018YFB1500103), the National Natural Science Foundation of China (Grant Nos. 61674084), the Overseas Expertise Introduction Project for Discipline Innovation of Higher Education of China (Grant No. B16027), Tianjin Science and Technology Project (Grant No. 18ZXJMTG00220). Key R&D Program of Hebei Province (No. 19214301D).

Conflict of interest statement: The authors declare no conflicts of interest regarding this article.

References

[1] K. Masuko, M. Shigematsu, T. Hashiguchi, et al., "Achievement of more than 25% conversion efficiency with crystalline silicon heterojunction solar cell," *IEEE J. Photovoltaics*, vol. 4, no. 6, pp. 1433–1435, 2014.

[2] J. Nakamura, N. Asano, T. Hieda, C. Okamoto, H. Katayama, and K. Nakamura, "Development of heterojunction back contact Si solar cells," *IEEE J. Photovoltaics*, vol. 4, no. 6, pp. 1491–1495, 2014.

[3] M. Taguchi, A. Yano, S. Tohoda, et al., "24.7% record efficiency HIT solar cell on thin silicon wafer," *IEEE J. Photovoltaics*, vol. 4, no. 1, pp. 96–99, 2014.

[4] D. Adachi, J. L. Hernández, and K. Yamamoto, "Impact of carrier recombination on fill factor for large area heterojunction crystalline silicon solar cell with 25.1% efficiency," *Appl. Phys. Lett.*, vol. 107, no. 23, p. 233506, 2015.

[5] K. Yoshikawa, H. Kawasaki, W. Yoshida, et al., "Silicon heterojunction solar cell with interdigitated back contacts for a photoconversion efficiency over 26%," *Nat. Energy*, vol. 2, no. 5, 2017.

[6] K. Yoshikawa, W. Yoshida, T. Irie, et al., "Exceeding conversion efficiency of 26% by heterojunction interdigitated back contact solar cell with thin film Si technology," *Sol. Energy Mater. Sol. Cells*, vol. 173, pp. 37–42, 2017.

[7] J. B. Heng, J. Fu, B. Kong, et al., "23% high-efficiency tunnel oxide junction bifacial solar cell with electroplated Cu gridlines," *IEEE J. Photovoltaics*, vol. 5, no. 1, pp. 82–86, 2015.

[8] F. Feldmann, M. Simon, M. Bivour, C. Reichel, M. Hermle, and S. W. Glunz, "Efficient carrier-selective p- and n-contacts for Si solar cells," *Sol. Energy Mater. Sol. Cells*, vol. 131, pp. 100–104, 2014.

[9] A. Richter, J. Benick, F. Feldmann, A. Fell, M. Hermle, and S. W. Glunz, "n-Type Si solar cells with passivating electron contact: identifying sources for efficiency limitations by wafer thickness and resistivity variation," *Sol. Energy Mater. Sol. Cells*, vol. 173, pp. 96–105, 2017.

[10] F. Haase, C. Hollemann, S. Schäfer, et al., "Laser contact openings for local poly-Si-metal contacts enabling 26.1%-efficient POLO-IBC solar cells," *Sol. Energy Mater. Sol. Cells*, vol. 186, pp. 184–193, 2018.

[11] F. Haase, S. Schafer, C. Klamt, et al., "Perimeter recombination in 25%-efficient IBC solar cells with passivating POLO contacts for both polarities," *IEEE J. Photovoltaics*, vol. 8, no. 1, pp. 23–29, 2018.

[12] K. Ding, U. Aeberhard, F. Finger, and U. Rau, "Silicon heterojunction solar cell with amorphous silicon oxide buffer and microcrystalline silicon oxide contact layers," *Phys. Status Solidi Rapid Res. Lett.*, vol. 6, no. 5, pp. 193–195, 2012.

[13] K. Ding, U. Aeberhard, F. Finger, and U. Rau, "Optimized amorphous silicon oxide buffer layers for silicon heterojunction solar cells with microcrystalline silicon oxide contact layers," *J. Appl. Phys.*, vol. 113, no. 13, p. 134501, 2013.

[14] K. Ding, U. Aeberhard, V. Smirnov, B. Holländer, F. Finger, and U. Rau, "Wide gap microcrystalline silicon oxide emitter for a-SiOx:H/c-Si heterojunction solar cells," *Jpn. J. Appl. Phys.*, vol. 52, no. 12R, p. 122304, 2013.

[15] A. Richter, F. Lentz, M. Meier, F. Finger, and K. Ding, "Light management in planar silicon heterojunction solar cells via nanocrystalline silicon oxide films and nano-imprint textures," *Phys. Status Solidi*, vol. 213, no. 7, pp. 1976–1982, 2016.

[16] M. Pomaska, A. Richter, F. Lentz, et al., "Wide gap microcrystalline silicon carbide emitter for amorphous silicon oxide passivated heterojunction solar cells," *Jpn. J. Appl. Phys.*, vol. 56, no. 2, p. 022302, 2017.

[17] T. Krajangsang, S. Inthisang, J. Sritharathikhun, et al., "An intrinsic amorphous silicon oxide and amorphous silicon stack passivation layer for crystalline silicon heterojunction solar cells," *Thin Solid Films*, vol. 628, pp. 107–111, 2017.

[18] C. Battaglia, S. M. de Nicolás, S. De Wolf, et al., "Silicon heterojunction solar cell with passivated hole selective MoO_x contact," *Appl. Phys. Lett.*, vol. 104, no. 11, p. 113902, 2014.

[19] J. Geissbühler, J. Werner, S. Martin de Nicolas, et al., "22.5% efficient silicon heterojunction solar cell with molybdenum oxide hole collector," *Appl. Phys. Lett.*, vol. 107, no. 8, p. 081601, 2015.

[20] A. Richter, M. Hermle, and S. W. Glunz, "Reassessment of the limiting efficiency for crystalline silicon solar cells," *IEEE J. Photovoltaics*, vol. 3, no. 4, pp. 1184–1191, 2013.

[21] I. Almansouri, A. Ho-Baillie, S. P. Bremner, and M. A. Green, "Supercharging silicon solar cell performance by means of multijunction concept," *IEEE J. Photovoltaics*, vol. 5, no. 3, pp. 968–976, 2015.

[22] M. Yamaguchi, K.-H. Lee, K. Araki, and N. Kojima, "A review of recent progress in heterogeneous silicon tandem solar cells," *J. Phys. D Appl. Phys.*, vol. 51, no. 13, p. 133002, 2018.

[23] S. Essig, C. Allebé, T. Remo, et al., "Raising the one-sun conversion efficiency of III–V/Si solar cells to 32.8% for two junctions and 35.9% for three junctions," *Nat. Energy*, vol. 2, no. 9, 2017.

[24] M. Green, E. Dunlop, J. Hohl-Ebinger, M. Yoshita, N. Kopidakis, and X. Hao, "Solar cell efficiency tables (version 57)," *Prog. Photovoltaics Res. Appl.*, vol. 29, no. 1, pp. 3–15, 2020.

[25] NREL. Available at: https://www.nrel.gov/pv/cell-efficiency.html.

[26] T. Leijtens, K. A. Bush, R. Prasanna, and M. D. McGehee, "Opportunities and challenges for tandem solar cells using metal halide perovskite semiconductors," *Nat. Energy*, vol. 3, no. 10, pp. 828–838, 2018.

[27] J. Werner, B. Niesen, and C. Ballif, "Perovskite/Silicon tandem solar cells: marriage of convenience or true love story? – An overview," *Adv. Mater. Interfaces*, vol. 5, no. 1, p. 1700731, 2017.

[28] I. J. Park, J. H. Park, S. G. Ji, M.-A. Park, J. H. Jang, and J. Y. Kim, "A three-terminal monolithic perovskite/Si tandem solar cell characterization platform," *Joule*, vol. 3, no. 3, pp. 807–818, 2019.

[29] F. Gota, M. Langenhorst, R. Schmager, J. Lehr, and U. W. Paetzold, "Energy yield advantages of three-terminal

perovskite-silicon tandem photovoltaics," *Joule*, vol. 4, no. 11, pp. 2387–2403, 2020.
[30] T. Tayagaki, K. Makita, T. Tachibana, et al., "Three-Terminal tandem solar cells with a back-contact-type bottom cell bonded using conductive metal nanoparticle arrays," *IEEE J. Photovoltaics*, vol. 10, no. 2, pp. 358–362, 2020.
[31] P. Tockhorn, P. Wagner, L. Kegelmann, et al., "Three-Terminal perovskite/silicon tandem solar cells with top and interdigitated rear contacts," *ACS Appl. Energy Mater.*, vol. 3, no. 2, pp. 1381–1392, 2020.
[32] M. Schnabel, H. Schulte-Huxel, M. Rienäcker, et al., "Three-terminal III–V/Si tandem solar cells enabled by a transparent conductive adhesive," *Sustain. Energy Fuels*, vol. 4, no. 2, pp. 549–558, 2020.
[33] H. Li and W. Zhang, "Perovskite tandem solar cells: from fundamentals to commercial deployment," *Chem. Rev.*, vol. 120, no. 18, pp. 9835–9950, 2020.
[34] A. Polman, M. Knight, E. C. Garnett, B. Ehrler, and W. C. Sinke, "Photovoltaic materials: present efficiencies and future challenges," *Science*, vol. 352, no. 6283, p. aad4424, 2016.
[35] D. Luo, R. Su, W. Zhang, Q. Gong, and R. Zhu, "Minimizing non-radiative recombination losses in perovskite solar cells," *Nat. Rev. Mater.*, vol. 5, no. 1, pp. 44–60, 2019.
[36] S. P. Philipps, F. Dimroth and A. W. Bett, *High-efficiency III–V Multijunction Solar Cells*, 2018, pp. 439–472, https://doi.org/10.1016/b978-0-12-809921-6.00012-4.
[37] C. Chen, Z. Song, C. Xiao, et al., "Achieving a high open-circuit voltage in inverted wide-bandgap perovskite solar cells with a graded perovskite homojunction," *Nanomater. Energy*, vol. 61, pp. 141–147, 2019.
[38] M. Saliba, T. Matsui, K. Domanski, et al., "Incorporation of rubidium cations into perovskite solar cells improves photovoltaic performance," *Science*, vol. 354, no. 6309, pp. 206–209, 2016.
[39] M. Lozac'h, S. Nunomura, and K. Matsubara, "Double-sided TOPCon solar cells on textured wafer with ALD SiO_x layer," *Sol. Energy Mater. Sol. Cells*, vol. 207, p. 110357, 2020.
[40] J. Bullock, Y. Wan, Z. Xu, et al., "Stable dopant-free asymmetric heterocontact silicon solar cells with efficiencies above 20%," *ACS Energy Lett.*, vol. 3, no. 3, pp. 508–513, 2018.
[41] C. Battaglia, A. Cuevas, and S. De Wolf, "High-efficiency crystalline silicon solar cells: status and perspectives," *Energy Environ. Sci.*, vol. 9, no. 5, pp. 1552–1576, 2016.
[42] L. Mazzarella, Y. H. Lin, S. Kirner, et al., "Infrared light management using a nanocrystalline silicon oxide interlayer in monolithic perovskite/silicon heterojunction tandem solar cells with efficiency above 25%," *Adv. Energy Mater.*, vol. 9, no. 14, p. 1803241, 2019.
[43] J. Bullock, M. Hettick, J. Geissbühler, et al., "Efficient silicon solar cells with dopant-free asymmetric heterocontacts," *Nat. Energy*, vol. 1, no. 3, 2016, https://doi.org/10.1038/nenergy.2015.31.
[44] X. Yang, K. Weber, Z. Hameiri, and S. De Wolf, "Industrially feasible, dopant-free, carrier-selective contacts for high-efficiency silicon solar cells," *Prog. Photovoltaics Res. Appl.*, vol. 25, no. 11, pp. 896–904, 2017.
[45] R. Cariou, J. Benick, F. Feldmann, et al., "III–V-on-silicon solar cells reaching 33% photoconversion efficiency in two-terminal configuration," *Nat. Energy*, vol. 3, no. 4, pp. 326–333, 2018.
[46] K. Makita, H. Mizuno, T. Tayagaki, et al., "III-V//Si multijunction solar cells with 30% efficiency using smart stack technology with Pd nanoparticle array," *Prog. Photovoltaics Res. Appl.*, vol. 28, no. 1, pp. 16–24, 2019.
[47] D. Lackner, O. Höhn, R. Müller, et al., "Two-Terminal direct wafer-bonded GaInP/AlGaAs//Si triple-junction solar cell with AM1.5g efficiency of 34.1%," *Sol. RRL*, vol. 4, no. 9, p. 2000210, 2020.
[48] A. Ingenito, G. Nogay, Q. Jeangros, et al., "A passivating contact for silicon solar cells formed during a single firing thermal annealing," *Nat. Energy*, vol. 3, no. 9, pp. 800–808, 2018.
[49] M. Rienäcker, M. Schnabel, E. L. Warren, A. Merkle, and R. Peibst, "Mechanically stacked dual-junction and triple-junction III–V/Si-IBC cells with efficiencies of 31.5 % and 35.4 %," in *33rd European Photovoltaic Solar Energy Conference and Exhibition*, 2017.
[50] A. Al-Ashouri, E. Khnen, B. Li, A. Magomedov, and S. Albrecht, "Monolithic perovskite/silicon tandem solar cell with >29% efficiency by enhanced hole extraction," *Science*, vol. 370, no. 6522, 2020, https://doi.org/10.1126/science.abd4016.
[51] E. Lamanna, F. Matteocci, E. Calabrò, et al., "Mechanically stacked, two-terminal graphene-based perovskite/silicon tandem solar cell with efficiency over 26%," *Joule*, vol. 4, no. 4, pp. 865–881, 2020.
[52] J. Xu, C. C. Boyd, Z. J. Yu, A. F. Palmstrom, and M. D. Mcgehee, "Triple-halide wide–band gap perovskites with suppressed phase segregation for efficient tandems," *Science*, vol. 367, no. 6482, pp. 1097–1104, 2020.
[53] B. Chen, Z. J. Yu, S. Manzoor, et al., "Blade-coated perovskites on textured silicon for 26%-efficient monolithic perovskite/silicon tandem solar cells," *Joule*, vol. 4, no. 4, pp. 850–864, 2020.
[54] D. Kim, H. J. Jung, I. J. Park, et al., "Efficient, stable silicon tandem cells enabled by anion-engineered wide-bandgap perovskites," *Science*, vol. 368, no. 6487, pp. 155–160, 2020.
[55] E. Köhnen, M. Jošt, A. B. Morales-Vilches, et al., "Highly efficient monolithic perovskite silicon tandem solar cells: analyzing the influence of current mismatch on device performance," *Sustain. Energy Fuels*, vol. 3, no. 8, pp. 1995–2005, 2019.
[56] Y. Hou, E. Aydin, M. D. Bastiani, et al., "Efficient tandem solar cells with solution-processed perovskite on textured crystalline silicon," *Science*, vol. 367, no. 6482, pp. 1135–1140, 2020.
[57] M. Jošt, E. Köhnen, A. B. Morales-Vilches, et al., "Textured interfaces in monolithic perovskite/silicon tandem solar cells: advanced light management for improved efficiency and energy yield," *Energy Environ. Sci.*, vol. 11, no. 12, pp. 3511–3523, 2018.
[58] B. Chen, Z. Yu, K. Liu, et al., "Grain engineering for perovskite/silicon monolithic tandem solar cells with efficiency of 25.4%," *Joule*, vol. 3, no. 1, pp. 177–190, 2019.
[59] B. A. Kamino, B. Paviet-Salomon, S.-J. Moon, et al., "Low-Temperature screen-printed metallization for the scale-up of two-terminal perovskite–silicon tandems," *ACS Appl. Energy Mater.*, vol. 2, no. 5, pp. 3815–3821, 2019.
[60] F. Sahli, J. Werner, B. A. Kamino, et al., "Fully textured monolithic perovskite/silicon tandem solar cells with 25.2% power conversion efficiency," *Nat. Mater.*, vol. 17, no. 9, pp. 820–826, 2018.

[61] K. A. Bush, S. Manzoor, K. Frohna, et al., "Minimizing current and voltage losses to reach 25% efficient monolithic two-terminal perovskite–silicon tandem solar cells," *ACS Energy Lett.*, vol. 3, no. 9, pp. 2173–2180, 2018.
[62] S. Zhu, F. Hou, W. Huang, et al., "Solvent engineering to balance light absorbance and transmittance in perovskite for tandem solar cells," *Sol. RRL*, vol. 2, no. 11, p. 1800176, 2018.
[63] F. Sahli, B. A. Kamino, J. Werner, et al., "Improved optics in monolithic perovskite/silicon tandem solar cells with a nanocrystalline silicon recombination junction," *Adv. Energy Mater.*, vol. 8, no. 6, p. 1701609, 2018.
[64] K. A. Bush, A. F. Palmstrom, Z. J. Yu, et al., "23.6%-efficient monolithic perovskite/silicon tandem solar cells with improved stability," *Nat. Energy*, vol. 2, no. 4, 2017.
[65] J. Werner, L. Barraud, A. Walter, et al., "Efficient near-infrared-transparent perovskite solar cells enabling direct comparison of 4-terminal and monolithic perovskite/silicon tandem cells," *ACS Energy Lett.*, vol. 1, no. 2, pp. 474–480, 2016.
[66] S. Albrecht, M. Saliba, J. P. Correa Baena, et al., "Monolithic perovskite/silicon-heterojunction tandem solar cells processed at low temperature," *Energy Environ. Sci.*, vol. 9, no. 1, pp. 81–88, 2016.
[67] J. Werner, C. H. Weng, A. Walter, et al., "Efficient monolithic perovskite/silicon tandem solar cell with cell area >1 cm(2)," *J. Phys. Chem. Lett.*, vol. 7, no. 1, pp. 161–6, 2016.
[68] B. Chen, S. W. Baek, Y. Hou, et al., "Enhanced optical path and electron diffusion length enable high-efficiency perovskite tandems," *Nat. Commun.*, vol. 11, no. 1, p. 1257, 2020.
[69] Z. Wang, X. Zhu, S. Zuo, et al., "27%-Efficiency four-terminal perovskite/silicon tandem solar cells by sandwiched gold nanomesh," *Adv. Funct. Mater.*, vol. 30, no. 4, p. 1908298, 2019.
[70] A. Rohatgi, K. Zhu, J. Tong, et al., "26.7% efficient 4-terminal perovskite–silicon tandem solar cell composed of a high-performance semitransparent perovskite cell and a doped poly-Si/SiO_x passivating contact silicon cell," *IEEE J. Photovoltaics*, vol. 10, no. 2, pp. 417–422, 2020.
[71] E. Aydin, M. De Bastiani, X. Yang, et al., "Zr-Doped indium oxide (IZRO) transparent electrodes for perovskite-based tandem solar cells," *Adv. Funct. Mater.*, vol. 29, no. 25, p. 1901741, 2019.
[72] J. Peng, T. Duong, X. Zhou, et al., "Efficient indium-doped TiOxElectron transport layers for high-performance perovskite solar cells and perovskite-silicon tandems," *Adv. Energy Mater.*, vol. 7, no. 4, p. 1601768, 2017.
[73] B. Chen, Y. Bai, Z. Yu, et al., "Efficient semitransparent perovskite solar cells for 23.0%-efficiency perovskite/silicon four-terminal tandem cells," *Adv. Energy Mater.*, vol. 6, no. 19, p. 1601128, 2016.
[74] D. P. Mcmeekin, G. Sadoughi, W. Rehman, et al., "A mixed-cation lead mixed-halide perovskite absorber for tandem solar cells," *Science*, vol. 351, no. 6269, pp. 151–155, 2016.
[75] J. Werner, G. Dubuis, A. Walter, et al., "Sputtered rear electrode with broadband transparency for perovskite solar cells," *Sol. Energy Mater. Sol. Cells*, vol. 141, pp. 407–413, 2015.
[76] P. Loper, S. J. Moon, S. M. de Nicolas, et al., "Organic-inorganic halide perovskite/crystalline silicon four-terminal tandem solar cells," *Phys. Chem. Chem. Phys.*, vol. 17, no. 3, pp. 1619–29, 2015.
[77] G. E. Eperon, S. D. Stranks, C. Menelaou, M. B. Johnston, L. M. Herz, and H. J. Snaith, "Formamidinium lead trihalide: A broadly tunable perovskite for efficient planar heterojunction solar cells," *Energy Environ. Sci.*, vol. 7, no. 3, p. 982, 2014.
[78] J. W. Lee, D. J. Seol, A. N. Cho, and N. G. Park, "High-efficiency perovskite solar cells based on the black polymorph of HC(NH2)2 PbI3," *Adv. Mater.*, vol. 26, no. 29, pp. 4991–8, 2014.
[79] D. Bi, C. Yi, J. Luo, et al., "Polymer-templated nucleation and crystal growth of perovskite films for solar cells with efficiency greater than 21%," *Nat. Energy*, vol. 1, no. 10, 2016.
[80] T. M. Koh, K. Fu, Y. Fang, et al., "Formamidinium-Containing metal-halide: An alternative material for near-IR absorption perovskite solar cells," *J. Phys. Chem. C*, vol. 118, no. 30, pp. 16458–16462, 2013.
[81] Z. Li, M. Yang, J.-S. Park, S.-H. Wei, J. J. Berry, and K. Zhu, "Stabilizing perovskite structures by tuning tolerance factor: formation of formamidinium and cesium lead iodide solid-state alloys," *Chem. Mater.*, vol. 28, no. 1, pp. 284–292, 2015.
[82] B. Conings, A. Babayigit, M. T. Klug, et al., "A universal deposition protocol for planar heterojunction solar cells with high efficiency based on hybrid lead halide perovskite families," *Adv. Mater.*, vol. 28, no. 48, pp. 10701–10709, 2016.
[83] M. Saliba, T. Matsui, J. Y. Seo, et al., "Cesium-containing triple cation perovskite solar cells: improved stability, reproducibility and high efficiency," *Energy Environ. Sci.*, vol. 9, no. 6, pp. 1989–1997, 2016.
[84] C. Yi, J. Luo, S. Meloni, et al., "Entropic stabilization of mixed A-cation ABX3 metal halide perovskites for high performance perovskite solar cells," *Energy Environ. Sci.*, vol. 9, no. 2, pp. 656–662, 2016.
[85] D. Bi, W. Tress, M. I. Dar, P. Gao, and A. Hagfeldt, "Efficient luminescent solar cells based on tailored mixed-cation perovskites," *Sci. Adv.*, vol. 2, no. 1, pp. e1501170, 2016.
[86] A. R. Yusoff, H. P. Kim, X. Li, J. Kim, J. Jang, and M. K. Nazeeruddin, "Ambipolar triple cation perovskite field effect transistors and inverters," *Adv. Mater.*, vol. 29, no. 8, 2017, https://doi.org/10.1002/adma.201602940.
[87] Y. Ogomi, A. Morita, S. Tsukamoto, et al., "CH3NH3SnxPb(1-x)I3 perovskite solar cells covering up to 1060 nm," *J. Phys. Chem. Lett.*, vol. 5, no. 6, pp. 1004–11, 2014.
[88] Q. Chen, N. De Marco, Y. Yang, et al., "Under the spotlight: the organic–inorganic hybrid halide perovskite for optoelectronic applications," *Nano Today*, vol. 10, no. 3, pp. 355–396, 2015.
[89] H. J. Snaith, "Present status and future prospects of perovskite photovoltaics," *Nat. Mater.*, vol. 17, no. 5, pp. 372–376, 2018.
[90] J. P. Mailoa, C. D. Bailie, E. C. Johlin, et al., "A 2-terminal perovskite/silicon multijunction solar cell enabled by a silicon tunnel junction," *Appl. Phys. Lett.*, vol. 106, no. 12, p. 121105, 2015.
[91] M. Jaysankar, W. Qiu, M. van Eerden, et al., "Four-Terminal perovskite/silicon multijunction solar modules," *Adv. Energy Mater.*, vol. 7, no. 15, p. 1602807, 2017.
[92] C. D. Bailie, M. G. Christoforo, J. P. Mailoa, et al., "Semi-transparent perovskite solar cells for tandems with silicon and CIGS," *Energy Environ. Sci.*, vol. 8, no. 3, pp. 956–963, 2015.
[93] F. Guo, H. Azimi, Y. Hou, et al., "High-performance semitransparent perovskite solar cells with solution-processed silver nanowires as top electrodes," *Nanoscale*, vol. 7, no. 5, pp. 1642–9, 2015.
[94] H. Kanda, A. Uzum, H. Nishino, et al., "Interface optoelectronics engineering for mechanically stacked tandem solar cells based on perovskite and silicon," *ACS Appl. Mater. Interfaces*, vol. 8, no. 49, pp. 33553–33561, 2016.

[95] P. You, Z. Liu, Q. Tai, S. Liu, and F. Yan, "Efficient semitransparent perovskite solar cells with graphene electrodes," *Adv. Mater.*, vol. 27, no. 24, pp. 3632–8, 2015.
[96] T. Duong, N. Lal, D. Grant, et al., "Semitransparent perovskite solar cell with sputtered front and rear electrodes for a four-terminal tandem," *IEEE J. Photovoltaics*, vol. 6, no. 3, pp. 679–687, 2016.
[97] L. Felix, G. Marc A, A. Steve, et al., "In situ graphene doping as a route toward efficient perovskite tandem solar cells," *Phys. Status Solidi*, vol. 213, no. 7, pp. 1989–1996, 2016.
[98] Y. Yang, Q. Chen, Y. T. Hsieh, et al., "Multilayer transparent top electrode for solution processed perovskite/Cu(in,Ga)(Se,S)2 four terminal tandem solar cells," *ACS Nano*, vol. 9, no. 7, pp. 7714–21, 2015.
[99] K. A. Bush, C. D. Bailie, Y. Chen, et al., "Thermal and environmental stability of semi-transparent perovskite solar cells for tandems enabled by a solution-processed nanoparticle buffer layer and sputtered ITO electrode," *Adv. Mater.*, vol. 28, no. 20, pp. 3937–43, 2016.
[100] F. Fu, T. Feurer, T. P. Weiss, et al., "High-efficiency inverted semi-transparent planar perovskite solar cells in substrate configuration," *Nat. Energy*, vol. 2, no. 1, 2016, https://doi.org/10.1038/nenergy.2016.190.
[101] L. Xiong, Y. Guo, J. Wen, et al., "Review on the application of SnO2 in perovskite solar cells," *Adv. Funct. Mater.*, vol. 28, no. 35, p. 1802757, 2018.
[102] L. Calió, S. Kazim, P. M. Grtzel, and S. Ahmad, "Hole-transport materials for perovskite solar cells," *Angew. Chem. Int. Ed.*, vol. 55, no. 47, pp. 14522–14545, 2016.
[103] F. Jiang, T. Liu, B. Luo, et al., "A two-terminal perovskite/perovskite tandem solar cell," *J. Mater. Chem.*, vol. 4, no. 4, pp. 1208–1213, 2016.
[104] L. Zheng, J. Wang, Y. Xuan, et al., "A perovskite/silicon hybrid system with a solar-to-electric power conversion efficiency of 25.5%," *J. Mater. Chem.*, vol. 7, no. 46, pp. 26479–26489, 2019.
[105] Y. Bai, X. Meng, and S. Yang, "Interface engineering for highly efficient and stable planar p-i-n perovskite solar cells," *Adv. Energy Mater.*, vol. 8, no. 5, p. 1701883, 2018.
[106] M. Stolterfoht, P. Caprioglio, C. M. Wolff, et al., "The impact of energy alignment and interfacial recombination on the internal and external open-circuit voltage of perovskite solar cells," *Energy Environ. Sci.*, vol. 12, no. 9, pp. 2778–2788, 2019.
[107] Z. Zhang, Z. Li, L. Meng, S. Y. Lien, and P. Gao, "Perovskite-Based tandem solar cells: get the most out of the sun," *Adv. Funct. Mater.*, vol. 30, no. 38, p. 2001904, 2020.
[108] G. E. Eperon, T. Leijtens, K. A. Bush, et al., "Perovskite-perovskite tandem photovoltaics with optimized bandgaps," *Science*, vol. 354, no. 6314, pp. 861–865, 2016.
[109] F. Fu, T. Feurer, T. Jager, et al., "Low-temperature-processed efficient semi-transparent planar perovskite solar cells for bifacial and tandem applications," *Nat. Commun.*, vol. 6, p. 8932, 2015.
[110] J. Urieta-Mora, I. Garcia-Benito, A. Molina-Ontoria, and N. Martin, "Hole transporting materials for perovskite solar cells: A chemical approach," *Chem. Soc. Rev.*, vol. 47, no. 23, pp. 8541–8571, 2018.
[111] Y. Kim, E. H. Jung, G. Kim, D. Kim, B. J. Kim, and J. Seo, "Sequentially fluorinated PTAA polymers for enhancing VOC of high-performance perovskite solar cells," *Adv. Energy Mater.*, vol. 8, no. 29, p. 1801668, 2018.
[112] A. G. Boldyreva, I. S. Zhidkov, S. Tsarev, et al., "Unraveling the impact of hole transport materials on photostability of perovskite films and p-i-n solar cells," *ACS Appl. Mater. Interfaces*, vol. 12, no. 16, pp. 19161–19173, 2020.
[113] Q. Jiang, X. Zhang, and J. You, "SnO2 : A wonderful electron transport layer for perovskite solar cells," *Small*, vol. 14, no. 31, p. e1801154, 2018.
[114] A. A. Said, J. Xie, and Q. Zhang, "Recent progress in organic electron transport materials in inverted perovskite solar cells," *Small*, vol. 15, no. 27, p. e1900854, 2019.
[115] S. Gharibzadeh, B. Abdollahi Nejand, M. Jakoby, et al., "Record open-circuit voltage wide-bandgap perovskite solar cells utilizing 2D/3D perovskite heterostructure," *Adv. Energy Mater.*, vol. 9, no. 21, p. 1803699, 2019.
[116] L. Deying, Y. Wenqiang, W. Zhiping, et al., "Enhanced photovoltage for inverted planar heterojunction perovskite solar cells," *Science*, vol. 360, no. 6396, pp. 1442–1446, 2018.
[117] M. Saliba, J. P. Correa-Baena, M. Gratzel, A. Hagfeldt, and A. Abate, "Perovskite solar cells: from the atomic level to film quality and device performance," *Angew Chem. Int. Ed. Engl.*, vol. 57, no. 10, pp. 2554–2569, 2018.
[118] Y. S. Kwon, J. Lim, H.-J. Yun, Y.-H. Kim, and T. Park, "A diketopyrrolopyrrole-containing hole transporting conjugated polymer for use in efficient stable organic–inorganic hybrid solar cells based on a perovskite," *Energy Environ. Sci.*, vol. 7, no. 4, p. 1454, 2014.
[119] B. Philippe, B.-W. Park, R. Lindblad, et al., "Chemical and electronic structure characterization of lead halide perovskites and stability behavior under different exposures—a photoelectron spectroscopy investigation," *Chem. Mater.*, vol. 27, no. 5, pp. 1720–1731, 2015.
[120] N. Aristidou, I. Sanchez-Molina Dr., T. Chotchuangchutchaval, et al., "The role of oxygen in the degradation of methylammonium lead trihalide perovskite photoactive layers," *Angew. Chem.*, vol. 54, no. 28, pp. 8208–8212, 2015.
[121] B. Conings, J. Drijkoningen, N. Gauquelin, et al., "Intrinsic thermal instability of methylammonium lead trihalide perovskite," *Adv. Energy Mater.*, vol. 5, no. 15, p. 1500477, 2015.
[122] S. R. Raga, M.-C. Jung, M. V. Lee, M. R. Leyden, Y. Kato, and Y. Qi, "Influence of air annealing on high efficiency planar structure perovskite solar cells," *Chem. Mater.*, vol. 27, no. 5, pp. 1597–1603, 2015.
[123] Z. Wang, D. P. McMeekin, N. Sakai, et al., "Efficient and air-stable mixed-cation lead mixed-halide perovskite solar cells with n-doped organic electron extraction layers," *Adv. Mater.*, vol. 29, no. 5, 2017, https://doi.org/10.1002/adma.201604186.
[124] S. Yang, W. Fu, Z. Zhang, H. Chen, and C.-Z. Li, "Recent advances in perovskite solar cells: efficiency, stability and lead-free perovskite," *J. Mater. Chem.*, vol. 5, no. 23, pp. 11462–11482, 2017.
[125] J. J. Yoo, S. Wieghold, M. C. Sponseller, et al., "An interface stabilized perovskite solar cell with high stabilized efficiency and low voltage loss," *Energy Environ. Sci.*, vol. 12, no. 7, pp. 2192–2199, 2019.
[126] R. Cariou, J. Benick, M. Hermle, D. Lackner, and F. Dimroth, "Development of highly-efficient III–V//Si wafer-bonded triple-junction solar cells," in *43rd IEEE Photovoltaic Specialists Conference (PVSC)*, IEEE, 2016.

[127] H. Shen, D. Walter, Y. Wu, et al., "Monolithic perovskite/Si tandem solar cells: pathways to over 30% efficiency," *Adv. Energy Mater.*, vol. 10, no. 13, p. 1902840, 2020.
[128] D. H. Kim, C. P. Muzzillo, J. Tong, et al., "Bimolecular additives improve wide-band-gap perovskites for efficient tandem solar cells with CIGS," *Joule*, vol. 3, no. 7, pp. 1734–1745, 2019.
[129] J. Rijcken, P. H. M. Bovendeerd, A. J. G. Schoofs, D. H. V. Campen, and T. Jimbo, "MOCVD growth of high efficiency current-matched AlGaAs/Si tandem solar cell," *J. Cryst. Growth*, vol. 174, no. 1, 1997.
[130] T. J. Grassman, D. J. Chmielewski, S. D. Carnevale, J. A. Carlin, and S. A. Ringel, "GaAsP/Si dual-junction solar cells grown by MBE and MOCVD," *IEEE*, pp. 326–331, 2017.
[131] T. Soga, T. Jimbo, and M. Umeno, "TEM characterization of antiphase domain in GaP on Si grown by MOCVD," *J. Cryst. Growth*, pp. 171–174, 1994.
[132] R. Cariou, J. Benick, P. Beutel, et al., "Monolithic two-terminal III–V//Si triple-junction solar cells with 30.2% efficiency under 1-sun AM1.5g," *IEEE J. Photovoltaics*, vol. 7, no. 1, pp. 367–373, 2017.
[133] M. T. Currie, S. B. Samavedam, T. A. Langdo, C. W. Leitz, and E. A. Fitzgerald, "Controlling threading dislocation densities in Ge on Si using graded SiGe layers and chemical-mechanical polishing," *Appl. Phys. Lett.*, vol. 72, no. 14, pp. 1718–1720, 1998.
[134] T. J. Grassman, J. A. Carlin, B. Galiana, et al., "Nucleation-related defect-free GaP/Si(100) heteroepitaxy via metal-organic chemical vapor deposition," *Appl. Phys. Lett.*, vol. 102, no. 14, p. 142102, 2013.
[135] A. Freundlich, L. Lombez, M. Sugiyama, et al., "1.7eV Al0.2Ga0.8As solar cells epitaxially grown on silicon by SSMBE using a superlattice and dislocation filters," *Spie Opto*, vol. 9743, p. 974310, 2016.
[136] N. Jain and M. K. Hudait, "III–V multijunction solar cell integration with silicon: present status, challenges and future outlook," *Energy Harvest. Syst.*, vol. 1, pp. 3–4, 2014.
[137] M. Feifel, D. Lackner, J. Ohlmann, J. Benick, M. Hermle, and F. Dimroth, "Direct growth of a GaInP/GaAs/Si triple-junction solar cell with 22.3% AM1.5g efficiency," *Sol. RRL*, vol. 3, no. 12, p. 1900313, 2019.
[138] J. B. Lasky, "Wafer bonding for silicon-on-insulator technologies," *Appl. Phys. Lett.*, vol. 48, no. 1, pp. 78–80, 1986.
[139] K. Petersen, P. Barth, J. Poydock, J. Brown, and J. Bryzek, "Silicon fusion bonding for pressure sensors," in *Solid-state Sensor and Actuator Workshop*, Hilton Head, Technical Digest, IEEE, 1988.
[140] K. Xiong, H. Mi, T.-H. Chang, et al., "AlGaAs/Si dual-junction tandem solar cells by epitaxial lift-off and print-transfer-assisted direct bonding," *Energy Sci. Eng.*, vol. 6, no. 1, pp. 47–55, 2018.
[141] K. N. Yaung, M. Vaisman, J. Lang, and M. L. Lee, "GaAsP solar cells on GaP/Si with low threading dislocation density," *Appl. Phys. Lett.*, vol. 109, no. 3, p. 032107, 2016.
[142] N. Shigekawa, T. Hara, T. Ogawa, et al., "GaAs/indium tin oxide/Si bonding junctions for III–V-on-Si hybrid multijunction cells with low series resistance," *IEEE J. Photovoltaics*, vol. 8, no. 3, pp. 1–8, 2018.
[143] P. Colter, B. Hagar, and S. Bedair, "Tunnel junctions for III–V multijunction solar cells review," *Crystals*, vol. 8, no. 12, p. 445, 2018.
[144] M. Hermle, G. Létay, S. P. Philipps, and A. W. Bett, "Numerical simulation of tunnel diodes for multi-junction solar cells," *Prog. Photovoltaics Res. Appl.*, vol. 16, no. 5, pp. 409–418, 2008.
[145] S. Wojtczuk, P. Chiu, X. Zhang, D. Pulver, C. Harris, and M. Timmons, "Bifacial growth InGaP/GaAs/InGaAs concentrator solar cells," *IEEE J. Photovoltaics*, vol. 2, no. 3, pp. 371–376, 2012.
[146] C. Ebert, Z. Pulwin, D. Byrnes, A. Paranjpe, and W. Zhang, "Tellurium doping of InGaP for tunnel junction applications in triple junction solar cells," *J. Cryst. Growth*, vol. 315, no. 1, pp. 61–63, 2011.
[147] J. Liang, S. Nishida, M. Morimoto, and N. Shigekawa, "Surface-activating-bonding-based low-resistance Si/III-V junctions," *Electron. Lett.*, vol. 49, no. 13, pp. 830–832, 2013.
[148] J. Liang, L. Chai, S. Nishida, M. Morimoto, and N. Shigekawa, "Investigation on the interface resistance of Si/GaAs heterojunctions fabricated by surface-activated bonding," *Jpn. J. Appl. Phys.*, vol. 54, no. 3, p. 030211, 2015.
[149] H. Mizuno, K. Makita, T. Tayagaki, T. Mochizuki, T. Sugaya, and H. Takato, "High-efficiency III–V//Si tandem solar cells enabled by the Pd nanoparticle array-mediated "smart stack" approach," *A*, vol. 10, no. 7, p. 072301, 2017.
[150] S. Essig, S. Ward, M. A. Steiner, et al., "Progress towards a 30% efficient GaInP/Si tandem solar cell," *Energy Procedia*, vol. 77, pp. 464–469, 2015.
[151] S. Essig, M. A. Steiner, C. Allebe, et al., "Realization of GaInP/Si dual-junction solar cells with 29.8% 1-sun efficiency," *IEEE J. Photovoltaics*, vol. 6, no. 4, pp. 1012–1019, 2016.
[152] E. Veinberg-Vidal, L. Vauche, K. Medjoubi, et al., "Characterization of dual-junction III-V on Si tandem solar cells with 23.7% efficiency under low concentration," *Prog. Photovoltaics Res. Appl.*, vol. 27, no. 7, pp. 652–661, 2019.
[153] M. Feifel, J. Ohlmann, J. Benick, et al., "Direct growth of III–V/silicon triple-junction solar cells with 19.7% efficiency," *IEEE J. Photovoltaics*, vol. 8, no. 6, pp. 1590–1595, 2018.
[154] T. Sugaya, T. Tayagaki, T. Aihara, et al., "Dual-junction GaAs solar cells and their application to smart stacked III–V//Si multijunction solar cells," *Appl. Phys. Express*, vol. 11, no. 5, p. 052301, 2018.
[155] H. Mizuno, K. Makita, T. Tayagaki, T. Mochizuki, and A. Ho-Baillie, "A "smart stack" triple-junction cell consisting of InGaP/GaAs and crystalline Si," in *2017 IEEE 44th Photovoltaic Specialists Conference (PVSC)*, IEEE, 2017.
[156] N. Shigekawa, J. Liang, R. Onitsuka, T. Agui, H. Juso, and T. Takamoto, "Current–voltage and spectral-response characteristics of surface-activated-bonding-based InGaP/GaAs/Si hybrid triple-junction cells," *Jpn. J. Appl. Phys.*, vol. 54, no. 8S1, p. 08KE03, 2015.
[157] S. Essig, J. Benick, M. Schachtner, A. Wekkeli, M. Hermle, and F. Dimroth, "Wafer-bonded GaInP/GaAs//Si solar cells with 30% efficiency under concentrated sunlight," *IEEE J. Photovoltaics*, vol. 5, no. 3, pp. 977–981, 2015.
[158] N. Shigekawa, L. Chai, M. Morimoto, J. Liang, and T. Takamoto, "Hybrid triple-junction solar cells by surface activate bonding of

III–V double-junction-cell heterostructures to ion-implantation-based Si cells," in *Photovoltaic Specialist Conference*, IEEE, 2014.

[159] F. Dimroth, T. Roesener, S. Essig, et al., "Comparison of direct growth and wafer bonding for the fabrication of GaInP/GaAs dual-junction solar cells on silicon," *IEEE J. Photovoltaics*, vol. 4, no. 2, pp. 620–625, 2014.

[160] K. Derendorf, S. Essig, E. Oliva, et al., "Fabrication of GaInP/GaAs//Si solar cells by surface activated direct wafer bonding," *IEEE J. Photovoltaics*, vol. 3, no. 4, pp. 1423–1428, 2013.

[161] K. Tanabe, K. Watanabe, and Y. Arakawa, "III–V/Si hybrid photonic devices by direct fusion bonding," *Sci*, vol. 2, p. 349, 2012.

[162] M. Baba, K. Makita, H. Mizuno, et al., "Feasibility study of two-terminal tandem solar cells integrated with smart stack, areal current matching, and low concentration," *Prog. Photovoltaics*, vol. 25, no. 3, pp. 255–263, 2017.